ELECTROMAGNETIC CONTROL OF THE HEAT AND MASS TRANFER PROCESSES IN GLAS-LIKE MATERIALS WITH NONLINEAR PROCESS INTERACTION AND RADIATIVE HEAT TRANSFER

Dr. Andris Jakovičs, Dr. Sergejs Pavlovs, Dr. Staņislavs Gendelis

1.LES modelling of heat and mass exchange in electrically conductive fluids for systems with complex configuration

Introduction

The channel induction furnace (CIF) is industrial metallurgical equipment with complex configuration of liquid region und high electrical and thermal efficiency. CIF is typically used for melting, holding and casting of metals and alloys, including cast iron and steel. Damages like erosion, clogging and infiltration of the ceramic lining in the channel as well as local overheating in the channel may lower the cleanness of the processed melt as well as the effectiveness and safety of CIF operation. The way to minimize these known problems is the choice of efficient regimes of melt circulation in CIF channel to provide controlled intensification of turbulent heat exchange between channel and throat.

As high temperature and flow velocity of the melt are extremely limiting the possibilities of experimental investigations of the heat and mass transfer and particle motion in CIF channel, the mathematical modelling based on Large Eddy Simulation (LES) approach is chosen for prediction of 3D transient temperature and velocity fields. The validity of LES approach has been verified by means of experimental and computational results' comparison obtained using experimental setups and CIF models. Then verified LES approach has been applied for long-term computations of industrial CIF properties including particles transport.

The main research activities and obtained results, published in [1–9], are the following.

1.1. CIF models under research

The models of industrial CIF under research consist of two groups:

• three models (fig. 1, 2, 3) have been developed for long-term study of heat and mass exchange in the melt;

• three models (fig. 4, 5, 6) have been introduces for computational estimation of influence of non-conductive build-up and sediments on electromagnetic (EM), turbulent hydrodynamic (HD) and thermal fields in the melt.

The peculiarities of the first group models are the following:

√ *Model 1* (fig. 1) with two symmetric channel branches represents the original design of CIF geometry;

√ *Model 2* (fig. 2) has gradual expansion of left channel branch from 100% to 200% of cross-sectional area at the junction to the throat;

√ *Model 3* (fig. 3) is the modification of the *Model 2* performed by a clockwise rotation by 90º angle of iron yoke from the original position, which is located around the right branch of channel, to the new one with location around the left branch of channel.

For *Models 1–3* the induced power in the melt is fixed at the level ~ 215 kW.

The peculiarities of the second group models are the following:

√ *Model 4* (fig. 4) has gradual narrowing of left channel branch from 100% to 25% of cross-sectional area at the junction to the throat, it simulates the build-up in the channel;
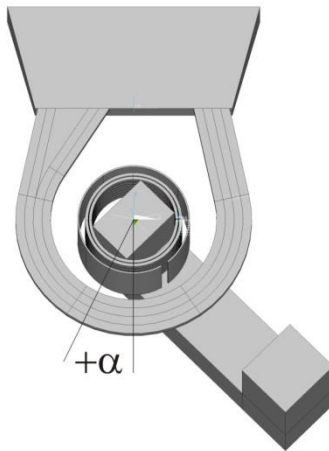
√ *Model 5* (fig. 5) has non-conductive sediments at the throat bottom in form of "hill";

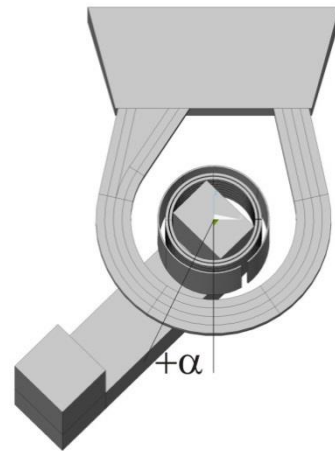√ *Model 6* (fig. 6) has non-conductive sediments at the throat bottom in form of "wall".

For *Models 4–6* the amplitude of current in inductor is fixed at the level 1850 A (number of turns – 28).
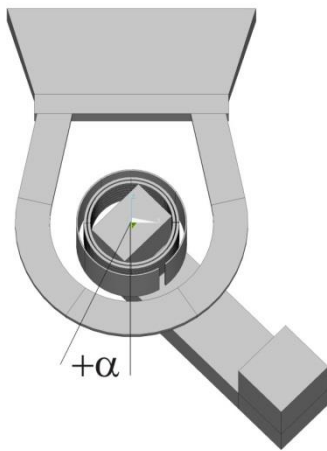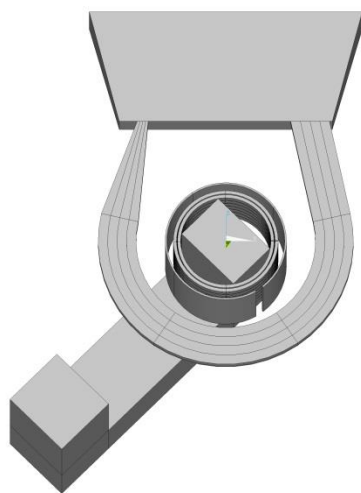

Fig. 1. Original geometry of CIF – symmetrical channel and position of iron yoke around the right channel branch
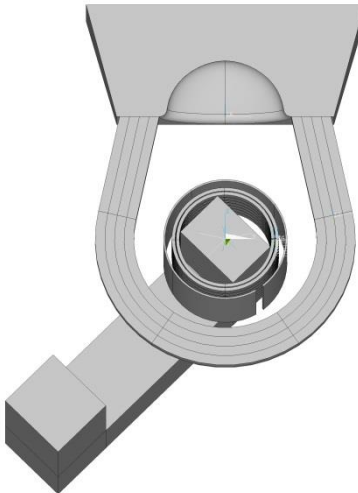

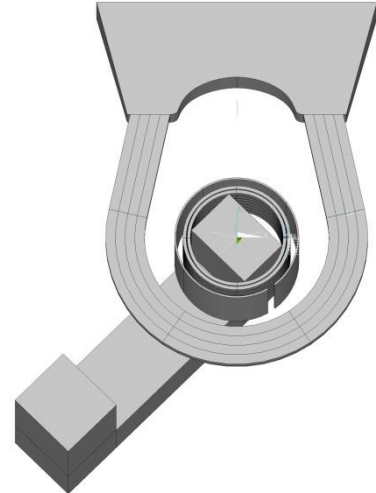*Fig. 2. CIF with widened left channel branch*

Fig. 3. CIF with widened left channel branch and rotated iron yoke to position around the left channel branch

Fig. 4. CIF with narrowed left channel branch, which simulates the build-up in the channel

Fig. 5. CIF with sediments at the throat bottom in form of "hill"

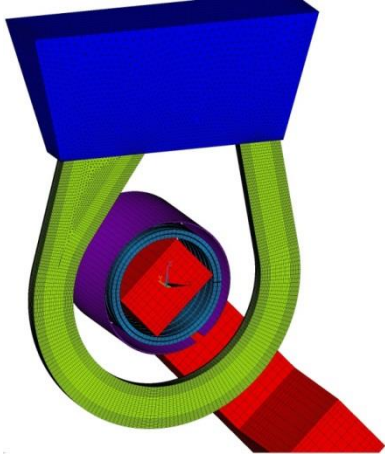*Fig. 6. CIF with sediments at the throat bottom in form of "wall"*

Fig. 7. Mesh for CIF with widened left channel branch created for elements of CIF construction for modelling of EM field
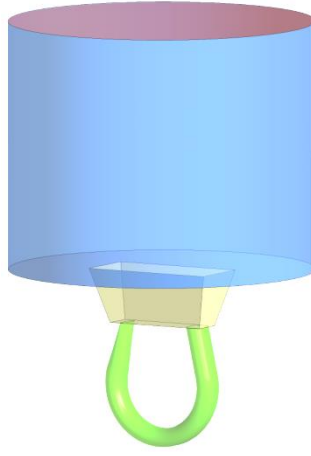
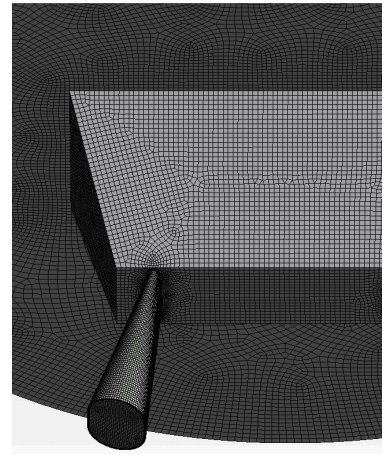*Fig. 8. Geometry of CIF with narrowed left channel branch for modelling of HD and thermal fields*

Fig. 9. Fragment of the mesh for modelling of HD and thermal fields in CIF with narrowed left channel branch

1.2. Peculiarities of computational process

The several variants of structures mesh (fig. 7, 9) have been developed for numerical modelling using PC cluster or mainstream desktop workstation (processor *Intel Core i7-2600,* 4-core (8-thread), 3.4 GHz, 8 GB of RAM) and commercial software packages:

√ *ANSYS Classic*, versions *11.0–14.0* for EM field computations (geometry of considered region is shown in fig. 7);

√ *ANSYS CFX*, versions *12.0–14.0* and *FLUENT*, version 6.2.6 for modelling of turbulent HD and thermal fields (geometry of considered region is shown in fig. 8).

The structured mesh (number of elements is up 1.5 million for EM field computations and 3–6 million for HD and thermal field computations) is developed and time step is chosen taking into account several limitations and requirements:

• mainstream desktop workstation's memory and performance limitations;

• CIF multi-zone geometry with extremely different levels of melt velocity value;

• contradictory properties of EM, HD and thermal boundary layers;

• LES approach application for computations of turbulent regime of melt flow in comparison with two parameters models of turbulence – k-ε or k-ω *SST* (*Shear Stress Transport*);

• application of hexahedral elements is preferable in place of tetrahedral ones.

1.3. Long-term computations of HD and thermal field in CIF with various designs

LES model of turbulence provides substantially more detailed results for HD and temperature distributions, which considerably differ from results obtained by k-ε model with respect to heat transfer processes and turbulent kinetic energy distributions:

• the quasi stable state in the temperature distribution (fig. 10a) for symmetrical CIF (fig. 1) obtained using *LES* modelling expressly differ from temperature distribution computed using k-ε model of turbulence;
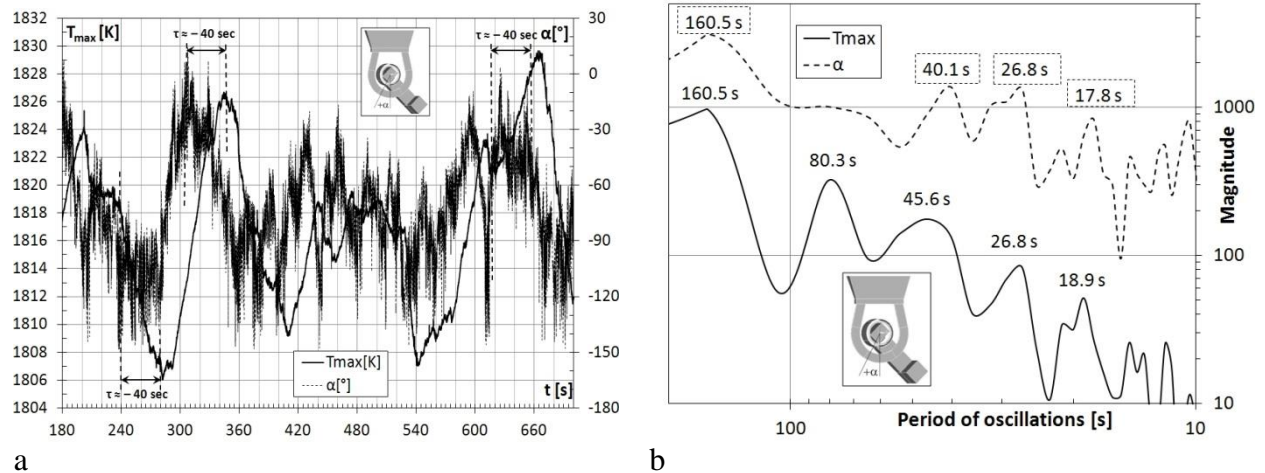
3

Fig. 10. CIF with symmetrical channel, cross-section y = 0, flow time interval t = 180–700 sec: (a) maximal temperature T$_{max}$ and angle α of its position; (b) results of FFT analysis for T$_{max}$ and α
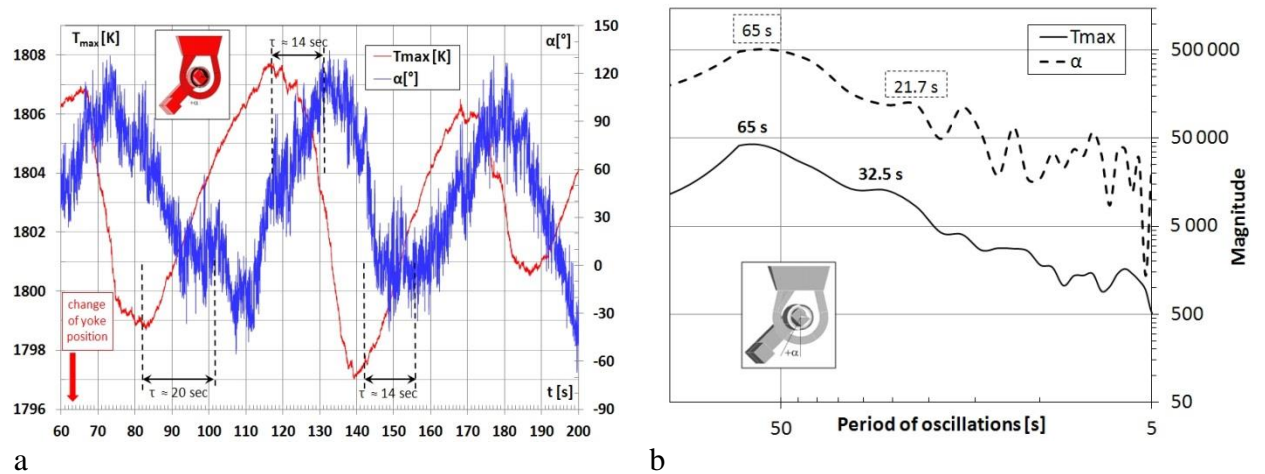

Fig. 11. CIF with widened channel branch, cross-section y = 0, flow time interval t = 60–200 sec: (a) maximal temperature T$_{max}$ and angle α of its position; (b) results of FFT analysis for T$_{max}$ and α

• the position of temperature maximum (fig. 11a) in asymmetrical CIF with widened channel branch (fig. 2, 3) obtained using k-ε model of turbulence only qualitatively corresponds to results obtained using *LES* method.

For industrial CIF the maximal temperature of the melt and its position in the channel have been analysed. For performed long-term computations there are not analogues in scientific publications – this research have been completed for the first time.

To reach quasi stable state of thermal field distribution in time (fig. 10a, 11a) it is necessary about several hundred seconds of flow time – for symmetrical CIF (fig. 1) almost 12 minutes (700 seconds) of flow time has been reached and for CIF with widened channel branch (fig. 2, 3) – more than 3 minutes (200 seconds).

The long-term modelling results' analysis using FFT (*Fast Fourier Transformation*) method makes it possible to fix the low-frequency oscillations of maximal temperature of the melt and its position in the channel with the following periods:

• for symmetrical CIF (fig. 1) – 160 seconds (fig. 10b);
• for CIF with widened channel branch (fig. 2, 3) – 65 seconds (fig. 11b).

4

It is essential, that these periods of oscillations are 3–4 times smaller than archived flow time interval.

The flow time intervals, archived during long-term computations, make it possible to fix the following effects for temperature field in CIF channel:

• the combination of both non-symmetrical factors (channel branch widening as well as iron yoke position changing) in one channel branch (fig. 3) results the long-term pulsations with more regular amplitude for all considered flow time interval;

• in symmetrical CIF (fig. 1) the pulsations of temperature maximum values lag in phase from temperature maximum position for the quarter of period (fig. 10a);

• in CIF with widened channel (fig. 2, 3) the pulsations of temperature maximum values advance in phase the temperature maximum position for the one fifth part of the period (fig. 11a);

• the values of time-averaged transit velocity for models with widened channel branch (fig. 2, 3) are for two orders smaller than maximum values of time-averaged velocity in cross-sections of CIF channel (fig. 13). Transit velocity is directed to the left widened channel branch. This branch is the region with better conditions for development of thermal-gravitational convection. It is the stronger factor, which enforces the temperature maximum to remain in the widened channel branch, if compare with the influence of EM sources' maxima position;

• there is the correlation between the position of temperature maximum in definite channel branch and transit velocity's direction to that very channel branch. In the case, when in start stage of computations the position of temperature maximum contradicts mentioned correlation, the change of temperature maximum position is fix – for symmetrical CIF (fig. 1) from the left channel branch to the right;

• CIF construction with moved yoke (fig. 3) provides the smaller overheating temperature in the channel in comparison with model (fig. 2) with the original yoke position.

1.4. Turbulent kinetic energy for re-circulated flows

√ For all cross-sections of CIF channel (fig. 13) the averaged flow patterns consist of two oppositely directed vortices with approximately equal intensity.

The LES computed distribution of instantaneous velocity (fig. 12a) in near wall mesh point between two oppositely directed vortices as well as spectrum of low frequency oscillations of instantaneous velocity (fig. 12b) are similar to experimental distributions for induction furnace for region between vortices (see above).

The character of turbulent kinetic energy distribution in zone of interaction of two oppositely directed vortices of the melt is similar for several MHD devices with so called re-circulated flows. It may be interpreted as universal regularity.

a   b
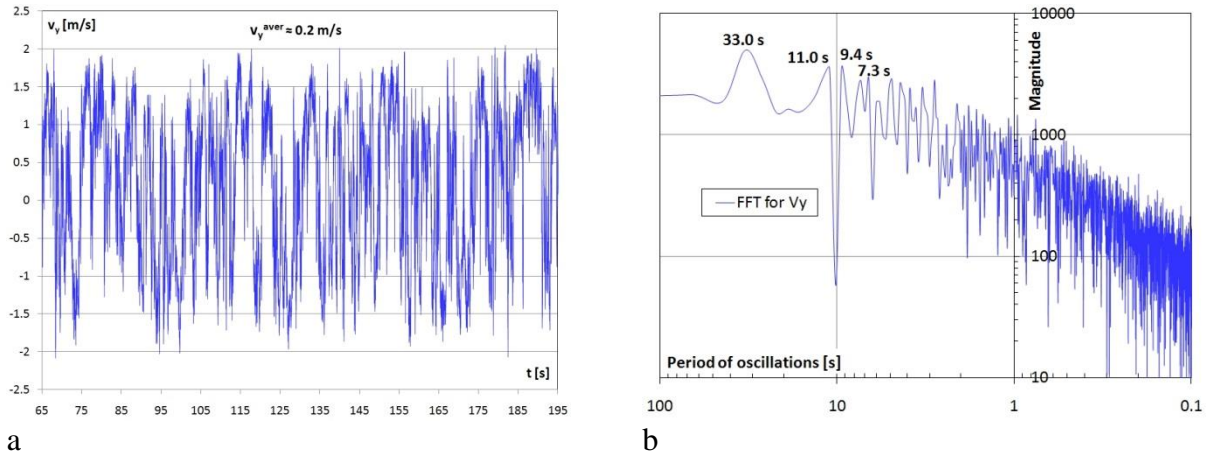
Fig. 12. CIF with widened channel, cross-section of outlet of left channel branch, near wall mesh point between two oppositely directed vortices, flow time t = 65–195 seconds:
(a) y-component of instantaneous velocity; (b) FFT analysis for y-component of velocity

1.5. CIF models with build-up of channel and clogging of throat

The structure of melt flow patterns in the channel (fig. 14a) for CIF with clogging of throat bottom (fig. 5, 6) is similar to flow structure in symmetrical CIF (fig. 1).

The sediments in throat noticeable change the melt flow structure in this zone (fig. 14b) because of throat effective height decrease.

The velocity values in throat zone increase because of effect of CIF channel conventional lengthen due to clogging of bottom zone, which may be interpreted as the shift of channel outlet to higher level.

For model with narrowed channel branch (fig. 4) due to decrease of cross-section area of channel with build-up according to *Bernoulli*'s principle for incompressible fluid the maximum values of instantaneous velocity are noticeable increasing (fig. 15) in zone of channel outlet as well as in throat zone near channel outlet.

The value of time-averaged transit velocity (fig. 19) in CIF model with narrowed channel branch (fig. 4) is smaller in comparison with symmetrical (fig. 1) and asymmetrical (fig. 2, 3) CIF. It may be interpreted as channel partly locking.

The clogging of throat bottom (fig. 5, 6) may be cause of noticeable concentration of Joule heat power in zones near sediments and thus may be cause of re-distribution of integral Joule heat power between various CIF zones.

The non-conductive sediments at the throat bottom may be cause of noticeable local overheating of melt, which may shorten the effective operation period of industrial CIF.

For model with narrowed channel branch (fig. 4) two zones of maxima of Joule heat power density are fixed:
• in the channel loop for zone near iron yoke;
• outlet zone of channel with build-up.

6
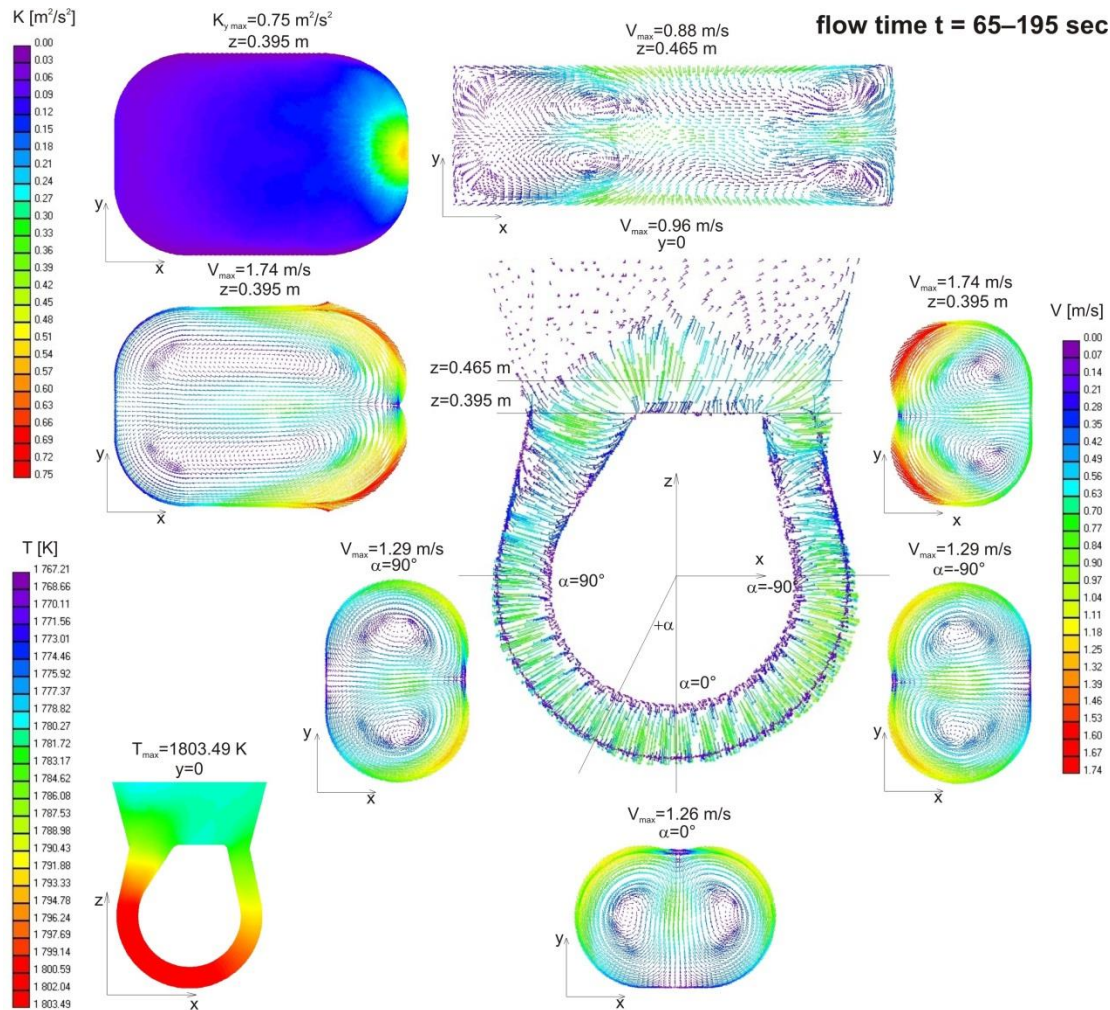
Fig. 13. CIF with widened channel, flow time t = 65–195 sec.Time-averaged velocity field for cross-sections: y = 0; z = 0.465 m; α = 0°; α = ±90°; z = 0.395 m (left and right channel outlets).Time-averaged turbulent pulsations of y-component of velocity for z = 0.395 m. Time-averaged temperature field for y = 0
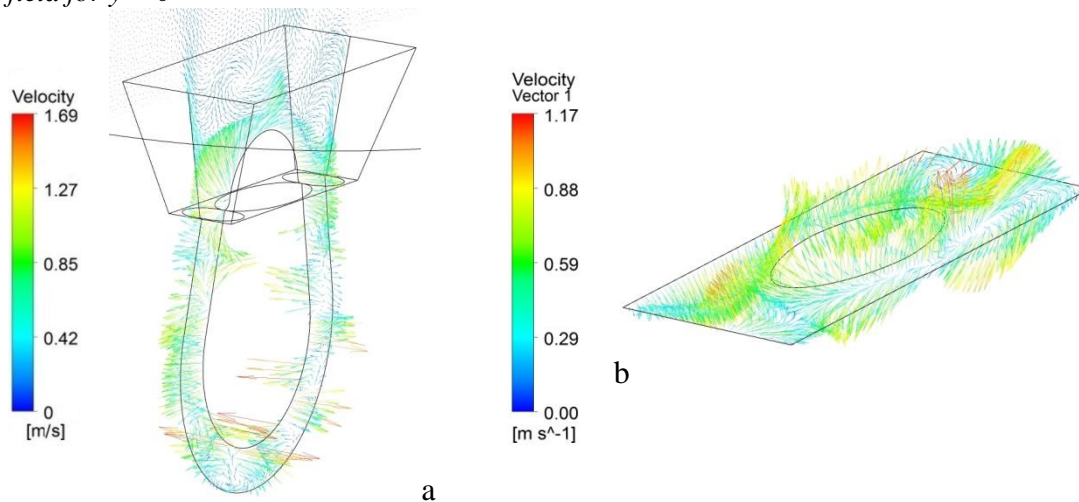
Fig. 14. CIF model with clogging of throat zone in form of "wall.
Instantaneous velocity field for flow time t = 10 s for cross-sections: (a) y=0; (b) z=0.45
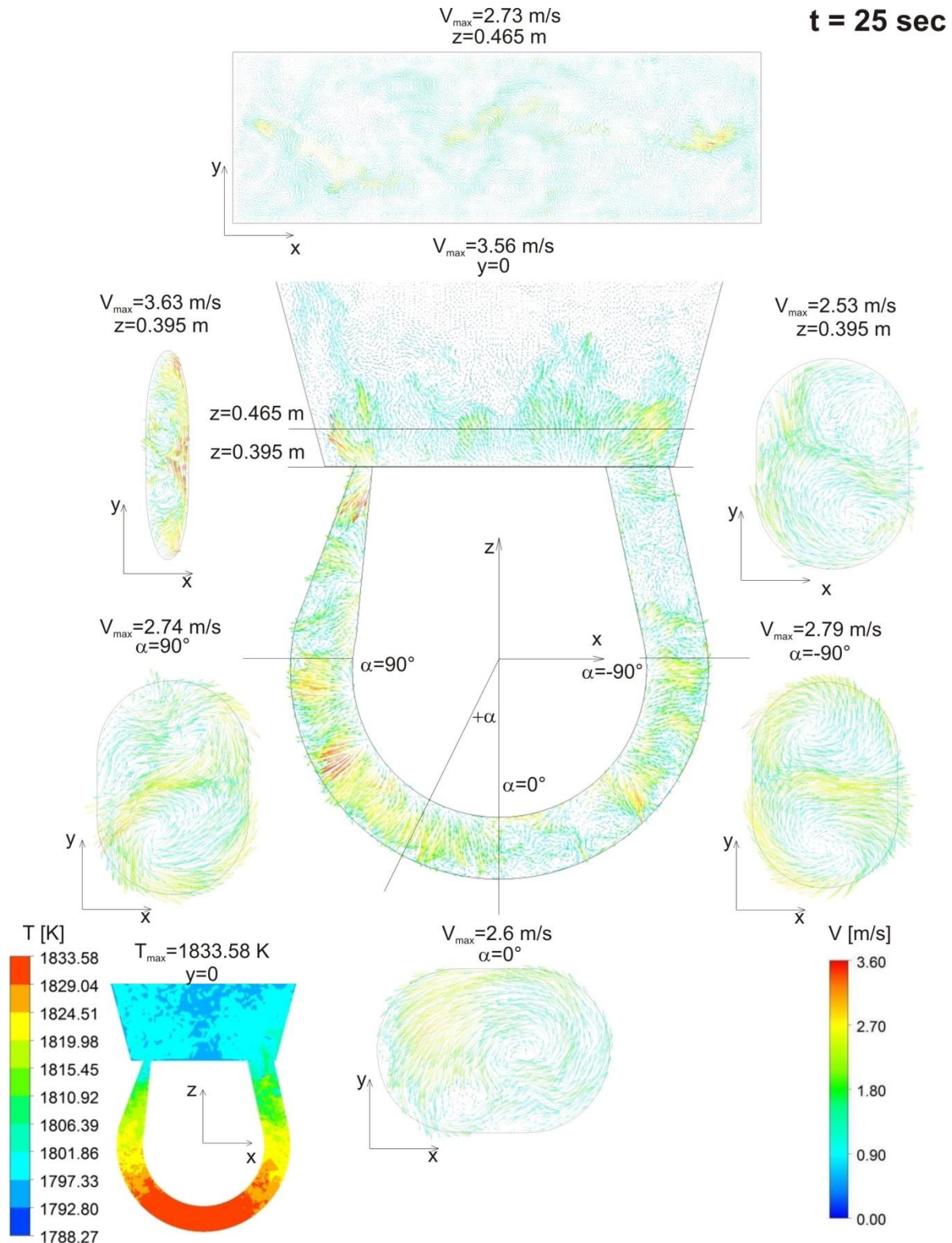
Fig. 15. CIF model with narrowed channel branch. Instantaneous velocity field for flow time t = 25 sec for cross-sections: y=0; z=0.465 m; x=0; α=0°; α=-90°; α=90°; z=0.395 m (outlets of left and right branch of channel). Instantaneous temperature field for flow time t = 25 sec for cross-section y=0

8
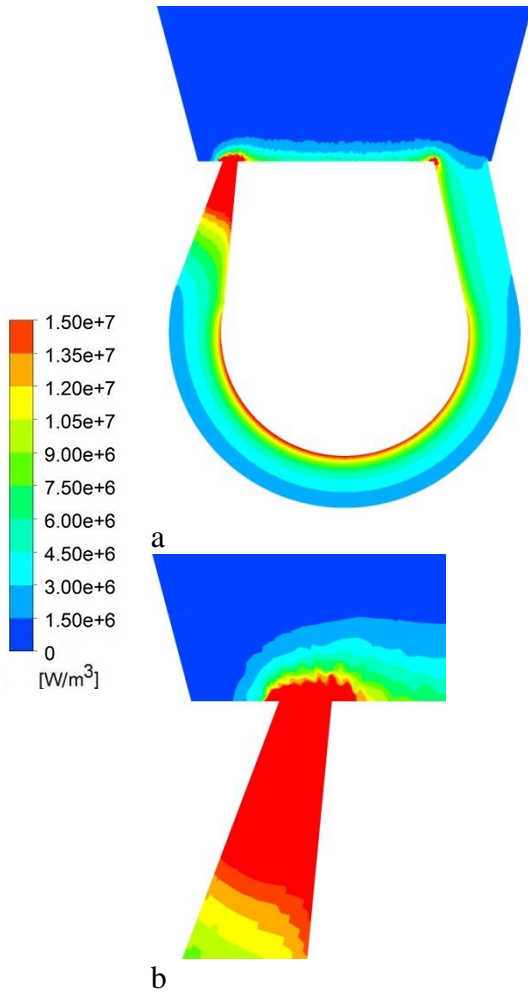
Fig. 16. CIF model with narrowed channel. Distribution of Joule heat density in cross-section y=0: (a) channel loop; (b) narrowed outlet zone.
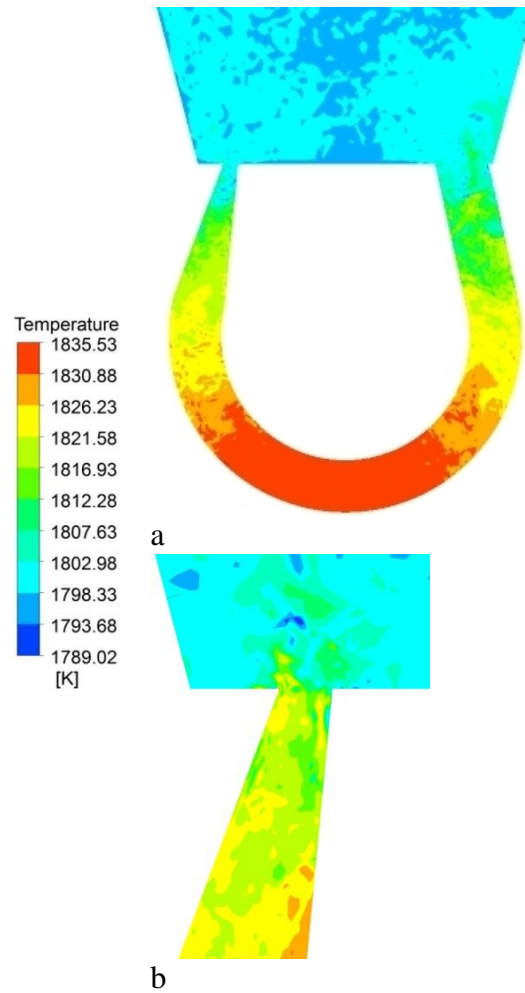
Fig. 17. Distribution of temperature field for flow time t = 20 seconds in cross-section y=0: (a) channel loop; (b) narrowed outlet zone
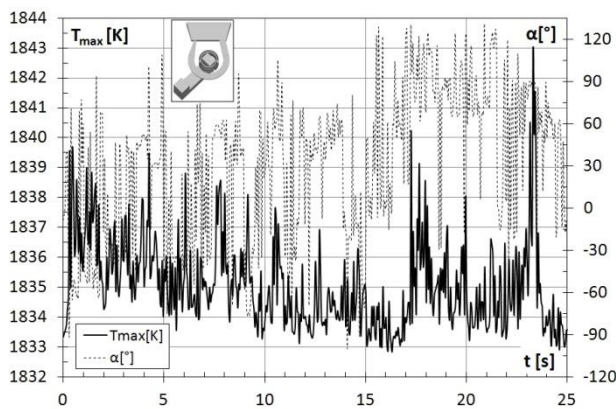
Fig. 18. CIF model with narrowed channel, cross-section y = 0 for flow time t = 0–25 seconds: maximal temperature T_{max} and angle α of its position
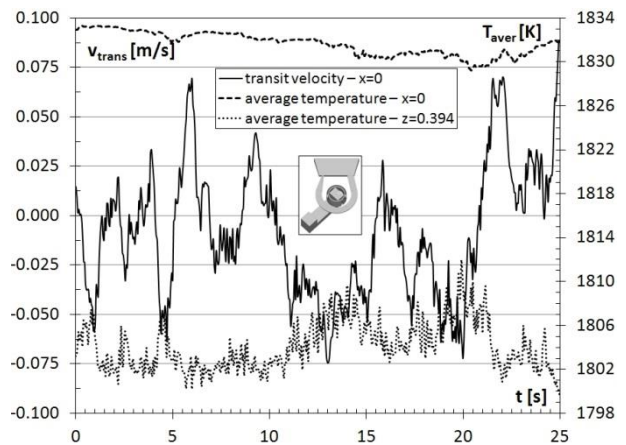
Att. 19. CIF model with narrowed channel for flow time t = 0–25 seconds: transit flow velocity for cross-section x=0 and averaged temperature for x=0 and z=0.394

The instantaneous temperature field has two zones of competitive maxima values which correspond to zones of maxima of Joule heat power density (fig. 17).

For archived by LES computations flow time interval t = 0–25 sec the development of two zones of averaged temperature, which correspond to zones of maxima of Joule heat power density, is not fixed (fig. 19).

Low frequency oscillations of maximum temperature and its position in channel (fig. 18) are not fixed up to now because the analysed flow time interval is noticeable shorter than expected period of oscillation.

1.6. Modelling of particle movement

For symmetrical CIF (fig. 1) and CIF with widened channel branch (fig. 2) the long-term computations of particles movement have been performed. The main assumptions regarding the particles' properties are the following:

   • particles are rigid spheres;
   • particles are electrically non-conductive;
   • particles do not affect the structure and velocities of the melt flow;
   • particle-particle interaction is negligible.
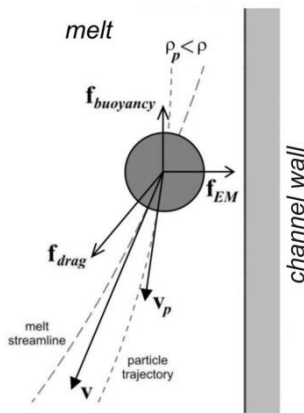
Fig. 20. Schemes of forces acting to light particle ($\rho_p < \rho$) near channel wall of CIF
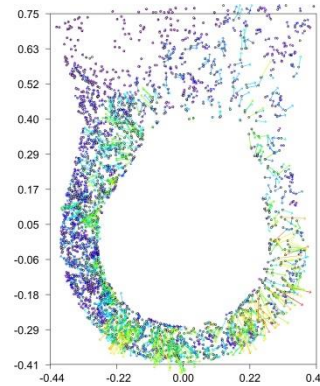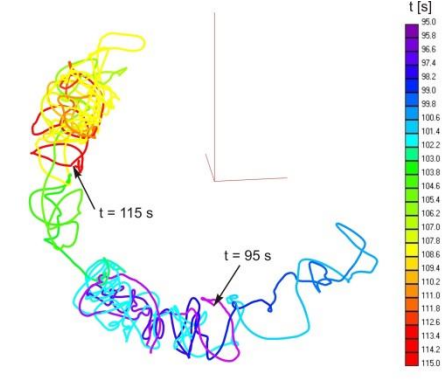
Fig. 21. CIF with widened channel:
(a) cloud particles' ($\rho_p \approx {}^3/_4 \rho_{melt}$) velocity vectors in the channel and in the throat for flow time t=125 seconds;
(b) track (coloured by time) of single particle ($\rho_p \approx {}^3/_4 \rho_{melt}$) for flow time t=95–115 seconds

The motion of the each particle is determined by integrating of movement equation taking into account the force balance (fig. 20):

   • *drag force* acting to particle is appeared due to melt viscosity;
   • *buoyancy force* acting to particle is appeared due to difference of particle and melt densities;
   • *electromagnetic force* acting to particle is appeared due to volumetric EM force in the melt.

The *Lagrangian* approach is used. It makes possible the computations of:

   • distribution in time of cloud of particles (fig. 22 and 23 right);
   • velocities of particles in cloud and separated particles (fig. 21a);
   • trajectories of separated particles (fig. 21b).

10
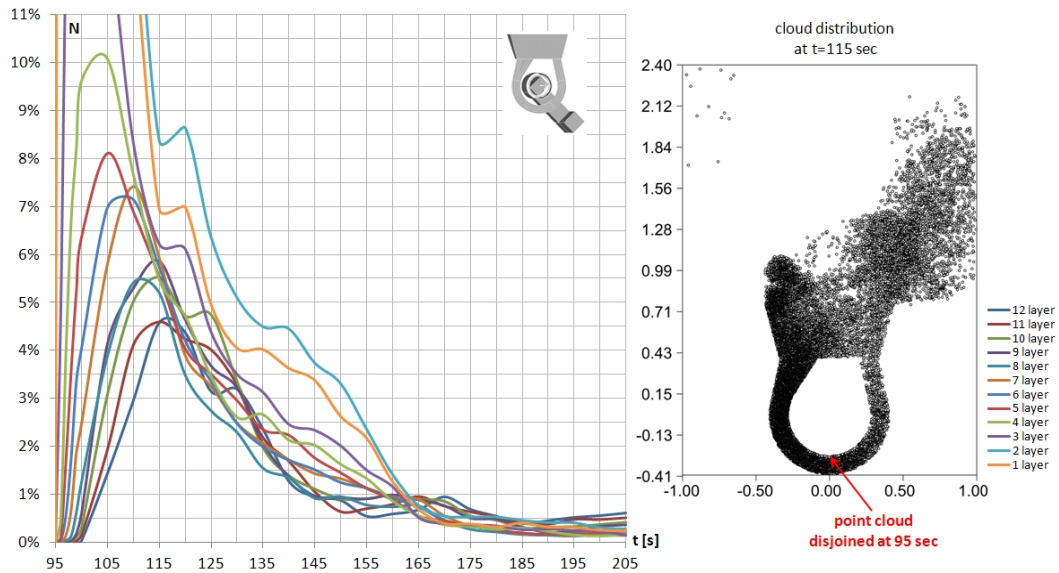
Fig. 22. CIF with widened channel, flow time interval 95–200 seconds:
(left) relative numbers of 25000 particles ($\rho_p \approx {}^3\!/_4\,\rho_{melt}$) cloud in channel and throat
for horizontal layers of equal thickness (see layers with numbers from 1 to 12 in right figure);
(right) distribution of particles cloud for flow time t=115 seconds
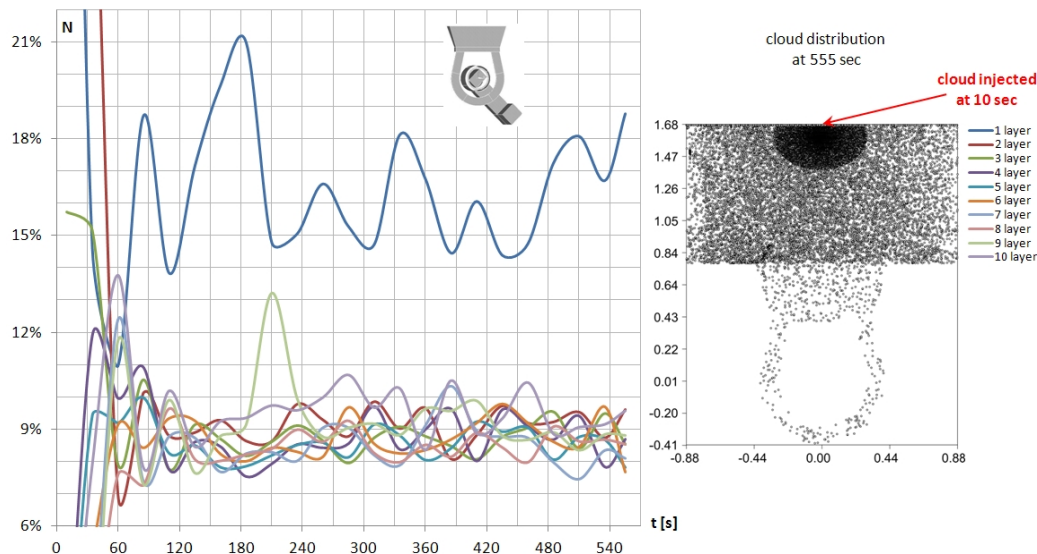
Fig. 23. CIF with symmetrical channel, flow time interval 10–555 seconds:
(left) relative numbers of 16000 particles ($\rho_p \approx {}^1\!/_4\,\rho_{melt}$) cloud in cylindrical bath
for horizontal layers of equal thickness (see layers with numbers from 1 to 10 in right figure);
(right) distribution of particles cloud for flow time t=555 seconds

The contamination rate of the melt has been estimated. Melt contamination appears due to disjoining of particle from ceramic lining wall due to channel erosion in high temperature melt.

The contamination rate is determined as the ratio of particles number, which have reached the bath, and total particles number, per unit of time flow (for example t = 1 min).

During the modelling of particles' cloud distribution for CIF with widened channel branch (fig. 2) the total flow time have been reached up to 2 minutes – t = 95–205 seconds.

The estimated contamination rate is ~ 85% (fig. 22).

11

Homogenization time of alloying additions has been estimated, when particles injected into melt are distributed approximately uniformly in the cylindrical bath.

During computations of particles' cloud distribution in symmetrical CIF (fig. 1) the total flow time have been reached almost 9 minutes – t = 10–555 seconds.

The estimated homogenisation time is ~ 2 min (fig. 23).

Conclusions

The validity of *LES* approach application for HD and thermal fields' modelling in CIF have been successfully verified by the comparison of experimental and computational results.

Performed long-term computations have shown the effectiveness of *LES* approach application for predictions of
- transient characteristics of turbulent heat exchange in industrial CIF;
- particle transport along the channel and in the bath.

There is a difficulty concerning the complex experimental verification of computational models of particles' transport in the high temperature non-transparent electrically conductive melts. This problem is not completely solved up to now.

References

[1] **Baake E., Jakovics A., Pavlovs S., Kirpo M**. *Numerical analysis of turbulent flow and temperature field in induction channel furnace with various channel design.* Proceedings of International Scientific Colloquium "Modelling for Material Processing", September 16–17, 2010, Riga, pp. 253–258.

[2] **Baake E., Jakovics A., Pavlovs S., Kirpo M**. *Long-term computations of turbulent flow and temperature field in induction channel furnace with various channel design.* Magnetohydrodynamics, 2010, Vol. 46, No. 4, pp. 317–330.

[3] **Baake E., Jakovics A., Pavlovs S., Kirpo M**. *Influence of the channel design on the heat and mass exchange of induction channel furnace.* The International Journal for Computation and Mathematics in Electrical and Electronic Engineering (COMPEL), 2011, Vol. 30, No. 5, pp. 1637–1650.

[4] **Jakovics A., Pavlovs S., Kirpo M., Baake E**. *Long-term LES study of turbulent heat and mass exchange in induction channel furnaces with various channel design.* Fundamental and applied MHD (Proceedings of 8th PAMIR International Conference on Fundamental and Applied MHD, September 5–9, 2011, Borgo, France). 2011, Vol. 1, pp. 283–288.

[5] **Pavlovs S., Jakovics A., Baake E., Nacke B., Kirpo M**. *LES modelling of turbulent flow, heat exchange and particles transport in industrial induction channel furnaces.* Magnetohydrodynamics, 2011, Vol. 47, No. 4, pp. 399–412.

[6] **Pavlovs S., Jakovics A., Baake E., Nacke B**. *LES long-term analysis of particles transport in melt turbulent flow for industrial induction channel furnaces.* Proceeding of 8th International Conference on Clean Steel, May 14–16, 2012, Budapest, Hungary. 12 p.

[7] **Pavlovs S., Jakovics A., Bosnyaks D., Baake E., Nacke B**. *Turbulent flow, heat and mass exchange in industrial induction channel furnaces with various channel design, iron yoke position and clogging.* Proceeding of the XVII Congress UIE-2012, May 21–25, 2012, Saint Petersburg, Russia, 8 p.

[8] **Jakovics A., Pavlovs S., Bosnyaks D., Spitans S., Baake E., Nacke B**. *Influence of channel and yoke design and clogging on turbulent flow and heat exchange in induction channel furnaces.* International Journal of Iron and Steel Research, 2012, Vol. 19, Supplement 1, pp. 749–753.

[9] **Nacke B., Baake E., Lupi S., Dughiero F., Forzan M., Barglik J., Dolega D., Jakovics A., Pavlovs S., Aliferov A**. Theoretical background and aspects of electrotechnologies. Physical principles and realization – St. Petersburg Electrotechnical university, 2012, 356 p.

2.Transport of solid inclusions in turbulent flow of liquid metal in alternate electromagnetic field

Introduction

The present work addresses the solid particles' transportation in the recirculated flow of metal melt in industrial induction metallurgical furnaces (IMF). All of them (induction crucible furnace – ICF, channel induction furnace – CIF, and others) have the same physical principle of operation (*Dötsch, 2009*) and, consequently, the similar flow distribution in the active region. The alternating current in the inductor creates a magnetic field and induces alternating current in the conductive liquid metal. The interaction of induced current and magnetic field results in the Lorentz force, which drives the liquid away from the wall and forms the two-eddy structure. However, the power of IMFs is sufficiently high to produce a turbulent flow with a high Reynolds number (e.g. for laboratory ICF it is about 1e+5). Therefore the mentioned two vortices appear only in the time averaged case, but in practice at each moment the turbulent flow consists of numerous eddies with different sizes, however, the common structure of the flow remains quasistationary (statistically stationary). The cross section of the ICF and the mean eddies are schematically shown on Figure 1 a.

The results produced by k-ε turbulence model, with a standard set of constants, show the highest values of turbulent kinetic energy in the eddy centers and the lowest between the eddies. Such distribution is characteristic for the k-ε model even in the case of 3D transient simulation (*Umbrashko et al., 2006*). However, the experimental results by *Umbrashko et al. (2006)* and *Kirpo et al. (2007)* show that the maximum of the turbulent energy is between the vortices of the averaged flow and close to the wall of the crucible. The average flow velocity in this area is close to zero, therefore the turbulent pulsations of velocity are large there. *Umbrashko et al. (2006)* and *Kirpo et al. (2007)* showed that the Large Eddy Simulation (LES) should be used for flow modeling in such equipment to achieve more realistic results. As far as the mass and heat transfer in the zone between eddies depends on the resolution of the velocity pulsations, the LES has to be used also for the objectives set out in the current paper. The spectrum of the pulsations of the axial velocity between these eddies has a clear low frequency maximum (*Umbrashko et al., 2006*). *Ščepanskis et al. (2011-a)* found the same maximum in the spectrum of the oscillations of the particle number in the zone between the mean eddies. However, the extreme parts of this spectrum differ from the spectrum of the flow velocity due to the inertial effects.

The flow inside the induction furnaces is sufficiently complex due to the presence of the electromagnetic (EM) forces. Therefore, the case described in this paper significantly differs from the well-studied turbulence in a pipe, a channel and other classical flows. It also differs from the turbulent flow in the gap between two counterrotating disks (the von Kármán flow) due to intensive axial pulsations between the main eddies near the wall that has already been discussed. Therefore, the behaviour of the particles in this type of a flow is interesting from an engineering point of view and yet has not been sufficiently researched. Moreover, the EM field directly influences the non-conducting particles in the conducting liquid within the penetration depth and transport them to the wall, which is another specific aspect of the considered system. The layer of significant EM field is sufficiently thin (about 20% of the radius of the crucible). Due to the non-slip boundary conditions the flow velocity is zero at the wall and increases dramatically in a radial direction until it achieves the maximal value. However, this maximum is in flows with high Reynolds numbers inside the layer of EM penetration. Obviously, particles

preferentially move in the streamline of maximal velocity. Therefore the major part of the particles come frequently to the layer of significant EM field. The particle motion in turbulent flows without EM is well researched, but it is not possible to separate the large interior zone without EM field from the thin layer near the wall and one should consider the motion of the particles in the whole volume.

EM heating and melting is one of the most effective methods for melting and processing of conducting materials. However, there is a problem of the homogenization of alloying particles, which are mixed in a steel melt to improve properties like strength, hardness and wear resistance. It is important to achieve homogeneous admixtures' distribution to ensure a high quality of the alloy. Furthermore, it is desirable to reduce the time of mixing to decrease the energy consumptions and prevent the melt from overheating. Most impurities and alloying elements have higher melting temperatures than metal. Thereby the melt can contain admixtures as solid particles. *Ščepanskis et al. (2010)* investigated the particle homogenization in ICF numerically.

Obviously, it is desirable to investigate the particle distribution in such systems experimentally, at least to verify the numerical model. But metals often have very high melting temperatures. Moreover, the electric well-conductive materials are not optically transparent, but transparent liquids have low conductivity. *Sadoway & Szekely (1980)* tried to use transparent LiCl-KCl eutectic to reproduce the recirculation motion in an ICF, but they met with failure. EM field does not only produce the induced flow motion, but also heat up the liquid within the penetration depth. Thereby the thermal convection dominates in the low-conductive transparent liquids. In spite of the optimistic conclusions of *Sadoway & Szekely (1980)*, the non-published simulation, which is done by the authors of the present paper, shows that it is not possible to avoid the thermal motion by changing the EM conditions. Therefore this liquid cannot be used to produce such flow patterns. The only more or less successful method, developed by *Taniguchi & Brimacombe (1994)*, provides an opportunity to investigate experimentally the rate of the particle deposition in a turbulent flow of liquid metal under EM force. However, because the results are obtained by cutting solidified liquid, it is impossible to receive any information about the dynamics of the process inside the melt using such experimental technique. Moreover, the presence of the solidification front has an influence on the particles during the solidification and it is not clear, if this effect is negligible.

Finally, the present paper proposes the original experimental technique, which uses ferromagnetic particles. This experiment allowed to verify the numerical model. The technique and the results are described in details below.

Previously *McKee et al. (1999)* proposed the greatly simplified analytical model for the calculation of the non-conductive particle path in rotating magnetohydrodynamic flow within a long cylinder. Later *Kirpo et al. (2009)* used Fluent software to investigate the behaviour of the particle cloud in the turbulent flows inside the induction furnaces. This model was sufficiently rough: only drag, buoyancy and EM forces were taken into account for the calculations of the particle motion. The model used by Kirpo was enhanced through development of OpenFOAM software code: the Lagrange equation was supplemented with lift, acceleration and added mass forces. The significance of these forces was statistically proved by *Ščepanskis et al. (2011-b)*.

2.1. Mathematical model
The present model includes the simulation of the flow and the particle motion. The flow is driven by EM force and thermal buoyancy force in the Boussinesq approximation. The turbulence is calculated using the Large Eddy Simulation (LES) method with the isotropic Smagorinsky subgrid viscosity model. The solid inclusions are calculated adopting the LES-based Euler-

Lagrange approach in the limit of dilute conditions (one-way coupling). This assumption is possible because the volume of the inclusions does not exceed 1% of the liquid volume. The rigid spheres are also assumed. The Lagrange equation describes the motion of the inertia non-conductive spherical particles (*Ščepanskis et al., 2011-b*):

$$\underbrace{\left(1 + \frac{C_A}{2}\frac{\rho_f}{\rho_p}\right)\frac{d u_p}{d t}}_{d u_p/d t + added\ mass\ force} = \underbrace{C_D \cdot U}_{drag\ force} + \underbrace{\left(1 - \frac{\rho_f}{\rho_p}\right) g}_{buoyancy\ force} - \underbrace{\frac{3}{8\rho_p}\mathbf{Re}\left(j_0 \times B_0^*\right)}_{EM\ force} + \underbrace{\frac{\rho_f}{\rho_p}C_L \xi}_{lift\ force} + \underbrace{\left(1 + \frac{C_A}{2}\frac{\rho_f}{\rho_p}\right)\frac{D u_f}{D t}}_{acceleration + added\ mass}, \quad (1)$$

where $U = u_f - u_p$, u_f and u_p are liquid and particle velocities respectively, ρ_f and ρ_p are liquid and particle density respectively, g is free fall acceleration; j_0 is the amplitude of current density, B_0^* is complex conjugated for the amplitude of magnetic flux, $\xi = U \times (\nabla \times U)$; $C_A (d U/d t, U)$, $C_D (U)$ and $C_L (U)$ are acceleration, drag and lift force coefficients respectively. The relevant approximations for the forces are chosen on the basis of the statistical analysis of the non-dimensional parameters (particle Reynolds number, shear stress and acceleration parameter).

It should be also mentioned that only the filtered velocity in the LES framework is known, and the isotropy of the subgrid part is assumed. Despite the calculation of the individual trajectories of particles, the analysis will be carried out for the cloud, therefore the unfiltered isotropic part of velocity should not influence the common results significantly.

As far as the hydrodynamics is simulated using the open source OpenFOAM software, the coupled Lagrange block is also programmed by means of OpenFOAM libraries. The particle tracking library is supplemented with EM, lift, acceleration and added mass forces. Thereby the Lagrange equation becomes non-linear. To ensure the convergence the hydrodynamic time step was split into various Lagrange time steps (LTS). The non-linear factors in the Lagrange equation are approximated with the values that correspond to the previous LTS (the Pikar's method). The implicit scheme is used to solve the equation. Moreover, the OpenFOAM algorithm does not take into account the collision of a particle with the wall in a situation when the size of the particle is larger than the size of a mesh element. If the distance between the particle centre and the wall is smaller than the radius, then the present model moves the particle to the distance of the radius from the wall at the end of the each LTS.

2.2. Experimental verification

The small 9 cm wide and 10 cm high crucible (that is the height of the melt) and the 4 kHz generator were used for the experiment (Figure 1 a). The spiral inductor had 6 turns and was the same height as the crucible. The 432 A current was applied in the inductor that corresponds to the induced power of 1.3 kW. The crucible was filled with the Wood's metal (50% Bi – 26.7% Pb – 13.3% Sn – 10% Cd eutectic), which becomes liquid at 70°C.

10.5 g of the spherical iron particles with diameter 250-350 μm were placed on the open surface of the liquid metal that generally corresponds to the industrial case of the admixing of alloying particles in ICF. The power of the furnace was switched on when the particles were already on the surface, it was done in the attempt to reduce the operation time of the furnace and thereby avoid the Wood's metal from dangerous overheating. Obviously, this case differs from industrial conditions, where the inclusions are usually placed on the surface of the already stirring metal. However, the measurements of the particle concentration were carried out at 11 s, when the transition regime of about 6 s had already passed. The local 4 ml probes of the particle laden Wood's metal were taken. Table 1 contains the comparison of the conditions in the experiment

15

and the simulation. The iron particles were collected from the liquid sample using a strong permanent magnet and counted after that.

Table 1: Comparison of the conditions in the experiment and the simulation

	Experiment	Simulation
Number (mass) of the particles	10.5±0.1 g (~1e+4 particles)	83 635 particles
Size of the particles	250 – 350 μm	300 μm
Material (density) of the particles	iron (Fe)	iron (7 874 kg/m^3)
Volume of the sample (experiment)	4±1 ml	-
Correspondence of the experimental and simulated results	number of particles in the sample	(number of particles in the proper region) × (vol. of the sample) / (volume of the proper region)

Generally, the time dependent EM force should be written as follows (the average expression of the force is placed in the equation (1)):

$$f = -\frac{3}{2}\frac{\sigma'' - \sigma'}{2\sigma'' + \sigma'}(j \times B) + \frac{\mu - \mu_0}{4\mu\mu_0}\nabla B^2, \quad (2)$$

where $j(t) = j_0 \sin(\omega t + \varphi)$ and $B(t) = B_0 \sin(\omega t + \varphi)$ are time dependent current density and magnetic flux respectively, σ'' and σ' are the conductivity of the liquid and the particle respectively, μ and μ_0 are the magnetic permeability of the particle and a vacuum respectively. The poor conductive ($\sigma' \ll \sigma''$) inclusions are usually used in the metallurgical applications, and they are non-magnetic ($\mu = \mu_0$). Thereby the equation (2) is reduced to the following expression:

$$f_1 = -\frac{3}{4}(j \times B) = -\frac{3}{4\mu_0}\left((B\nabla)B - \frac{1}{2}\nabla B^2\right). \quad (3)$$

In the area of the maximal magnetic flux – at the middle of the inductor – B_r and B_φ are negligible. Therefore the first term in (3) can be reduced to $3/(4\mu_0) \cdot e_z \cdot B_z \cdot \partial B_z/\partial z$ that is also negligible, because $\partial B_z/\partial z \approx 0$. Thus, the term $(B\nabla)B$ is much less than the second term in (3) at the middle of the inductor:

$$f_1 \approx \frac{3}{8\mu_0} \cdot \nabla B^2. \quad (4)$$

However, the iron particles are used in the experiment. Iron is a good conductor ($\sigma' > \sigma''$) and a ferromagnetic material ($\mu \gg \mu_0$), but due to the partial wetting and the transitional resistance we can assume the equal conductivity of the particle and the liquid. Therefore for this type of particles equation (2) can be reduced to

$$f_2 = \frac{1}{2\mu_0} \cdot \nabla B^2. \quad (5)$$

Apparently, the equation (4) and (5) shows that $f_1 \approx f_2$ at the middle of inductor. The results of the EM simulation on Figure 1 b also confirm the coincidence of the forces in the middle zone of the crucible, however, $f_2 \approx 3/2\, f_1$ in the zone of the flow vortices. Despite the non-critical differences between the forces f_1 and f_2 in the upper and lower eddies, it is possible to conclude that the iron particles can be used as the rough physical model of the typical metallurgical inclusions in the induction furnaces.

Figure 1 c provides comparison of the experimental results and the appropriate simulation. The simulation was carried out for the non-conductive and non-magnetic particles that corresponds to f_1. However, it must be noted that the iron particles, which are well-conductive and ferromagnetic, have been used in the experiment. The conditions and the rest EM parameters in the simulation are the same as in the physical experiment. 3 curves on the Figure 1 c correspond to the radial distribution of the inclusions at different depths: 3 cm (upper eddy), 5 cm (middle of the crucible) and 7 cm (lower eddy) from the surface. Notwithstanding the different conductivity and magnetic permeability of the inclusions, the experimental and simulated curves are in the satisfactory agreement to each other in all points except one: on the axis of symmetry in the zone of the upper eddy. This fact confirms the hypothesis discussed above and it is possible to use the iron particles as the physical model of non-conductive metallurgical inclusions.

However, two things should be additionally discussed concerning the results on Figure 1 c.

1. Unfortunately, no explanation has been obtained regarding the significant difference between experimental and simulated results in one point – on the symmetry axis in the upper part of the crucible. The experimental technology was quite rough and only 3 series of experiments yield the results on the upper curve of Figure 1 c. At the same time other experimental curves on Figure 1 c are drawn taking into account 4 – 10 experimental series. Therefore the problematic experimental point is the less reliable one compared to others.
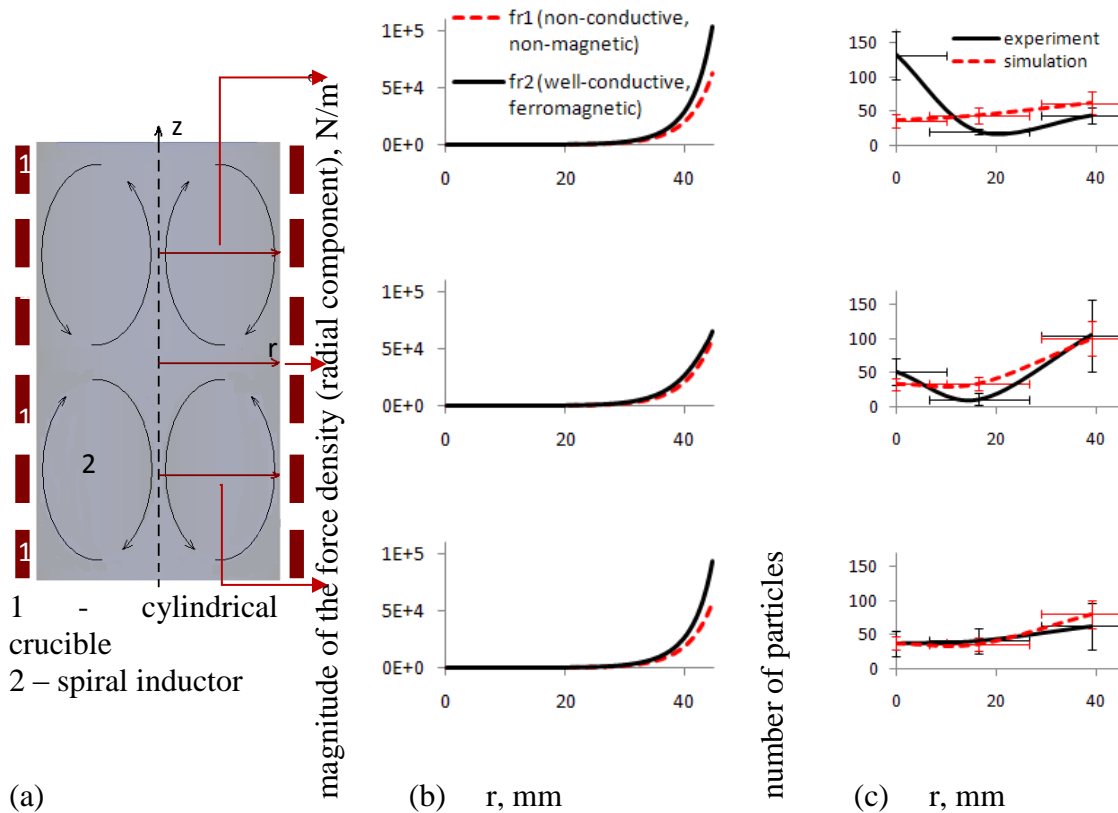
Fig 1: (a) scheme of ICF; (b) magnitude of the force density (radial component) in the case of non-conductive & non-magnetic and well-conductive & ferromagnetic particles (see equations (3) and (5) respectively); (c) the distribution of spherical 300±50 μm inclusions in ICF at 11±2 s from the beginning of stirring (quasi-stationary regime) at different depths from the surface (see the scheme of the crucible on the left).

2. The clustering of the particles on the wall in the zone of upper eddy was observed in the experiment. The authors believe that these clusters, which by the way contain the great number of particles, are formed due to EM force, which holds the particles on the wall. The simulation also shows the concentration of the inclusions on the wall. However, this clustering effect was obviously enforced by poor wetting and the surface tension on the liquid metal – particle – wall interface. To the extent that the clustered inclusions were held on the wall, these particles did not get into the samples and did not influence the experimental results. Therefore, the particles, which were situated directly on the wall, were removed from the simulated data on Figure 1 c.

Thus it is possible to conclude that 1) the numerical model is in the satisfactory agreement with the experimental results; 2) it is convenient to use the iron particles as a physical model of non-conductive particles in conductive liquid in vicinity of an EM field.

2.3. Industrially oriented results

Following the previous discussion, the numerical model was verified experimentally in ICF-1. Therefore it is possible to analyze the industrial full scale process numerically.

Carbon particles are the typical alloying inclusions in steel. According to the widespread induction technology, the carbon particles are placed on the open surface of the liquid metal in

the same ICF, where it has been melted previously. Then the intensive turbulent flow of alloy mixed the solid particles into the melt in spite of their low density. The carbon has a low conductivity, and moreover, transitional resistance appears on the surface. Therefore the EM force is applied in the Lagrange equation (1) as for a non-conductive particle.

Fig. 2 compares the simulation of the carbon admixing process in steel with the industrial observations. Since the liquid steel is not transparent and is extremely hot, it is possible to compare only the behaviour of the particles on the open surface of the steel during the initial stage of the process (Fig. 2 – first and second rows). The results qualitatively agree, therefore the motion in the bulk of the crucible can be analyzed, which is invisible (Fig. 2 – last row).

Moreover, the long period of initial admixing (particle disappearance from the surface) can be observed on Fig. 2. Fig. 3 illustrates the significance of the power, which is necessary to apply to take the inclusions into the melt even for the small ICF-1 (6 kg). Numerical modelling of such process should take into account the wettability of inclusions, surface tension and corner effects, which are poor research properties for many materials. Therefore the experimental investigation of this process taking into account Reynolds similarity principle is more convenient.

Another important challenge for the ICF operator is to realize the time of homogenization of inclusions in the bulk of the melt. The zero or minimal difference of the particle number $\varDelta N$ between the zones of the upper and the lower eddy (see Fig. 1a) is the goal of stirring process, however, it cannot be controlled. Fig. 4 illustrates the homogenization process, which can be divided in two stages [5]. The first stage of the homogenization corresponds to the time, when the initial cloud of the particles comes to the middle zone of the crucible by the wall, and is characterized with parameter $\delta(S,D)$. The second stage of slow homogenization is characterized by the exchange of particles between the zones of eddies and the parameter of linear regression $a(S,D)$.

The parameter of the initial stage of the homogenization δ decreases with increase of liquid-to-particle density ration S and increases with increase of diameter of inclusions D. Moreover, $\delta(S,D)$ and $a(S,D)$ for simulated curves of laboratory scale **ICF-2** (radius 15.8 cm, height of the melt 54 cm, current 2000A, frequency 365 Hz) can be approximated with the following linear regression:

$\delta(S,D) = 0.8 + 1.2\text{e-}3 \cdot D$ [µm] - $0.3 \cdot S,$ \qquad standard deviation: 4.6e-2; \qquad (3)
$a(S,D) = -1.5\text{e-}2 + 2.0\text{e-}5 \cdot D$ [µm] + $3.4\text{e-}3 \cdot S,$ \quad standard deviation: 6.8e-4. \qquad (4)

Initial stage of rapid homogenization takes $t_{1.st} = 7.3 \pm 1.2$ s from the beginning of admixing. And the total time of homogenization

$$t_{hom}(S,D) = t_{1.st} + t_{2.st}(S,D) = t_{1.st} + \frac{\left(\Delta N / N\right)_{\infty} + \delta(S,D) - 1}{a(S,D)}, \qquad (5)$$

where the asymptotic value $\left(\Delta N / N\right)_{\infty}$ is equal to zero, when $S=1$, and $(8.4 \pm 1.2)\text{e-}2$ otherwise.

Obviously, the coefficients in regression model (2-4) as well as results in Tab. 1 are relevant only for particular geometry and EM parameters of ICF-2. However, generally such methodology can be used for the optimization of ICF for stirring purpose.
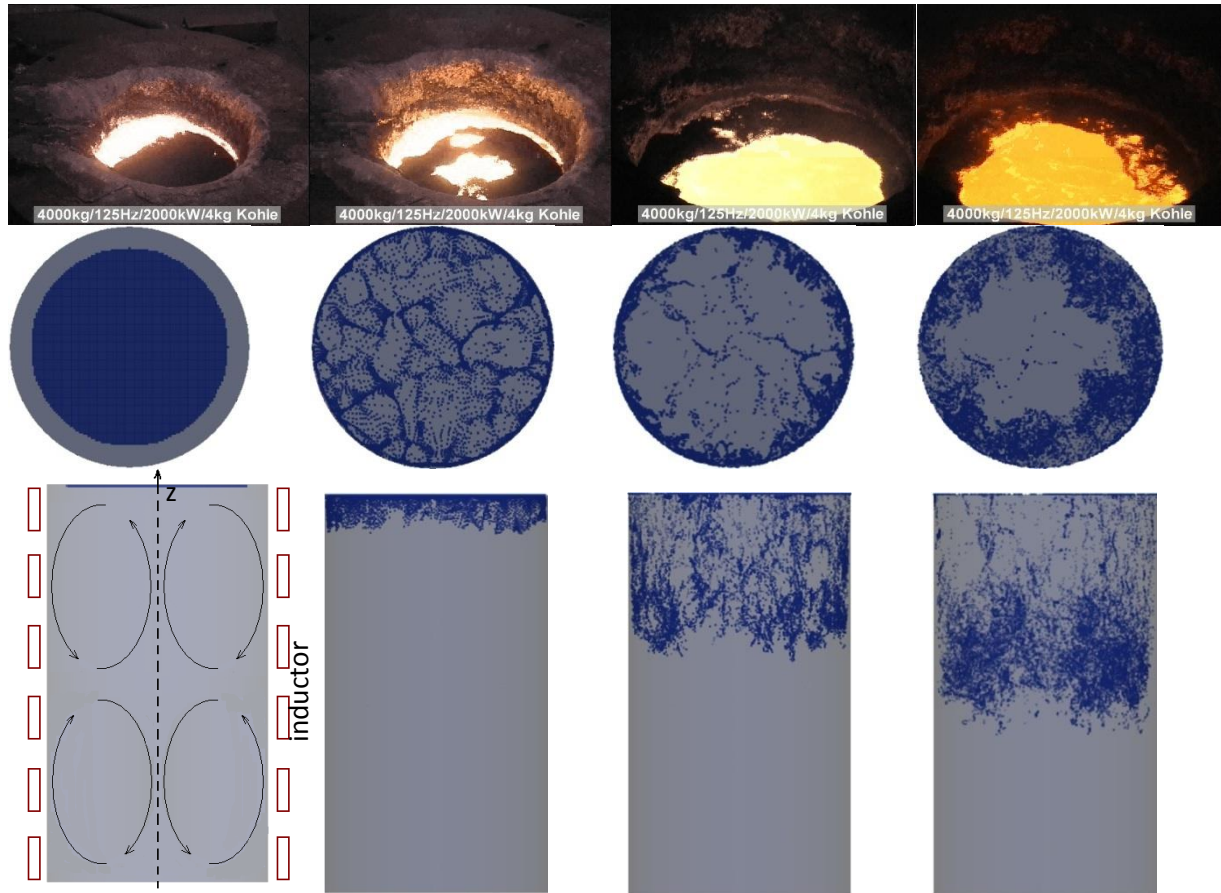
Fig. 2. The admixing of the 100 µm carbon particles into the steel alloy in ICF-2. Snapshots of industrial process by Otto Junker GmbH (first row). Simulated results: view from the top of the furnace (second row); particles in the bulk of the flow, view from the side of furnace (last row).

The last but not least important issue for the optimization of design and operation of ICF is deposition of large-size particle on the wall, which take place due to the direct influence of EM force on non-conducting particles. These particles are moved out of the alloy, therefore the significant deposition should be prevented. Fig. 5 illustrates the increase of the number of deposited particles with increase of liquid-to-particle density ratio S.

Power   1.3 kW   2.4 kW   3.7 kW

Fig. 3. The surface of the Wood's metal with iron particles after 10 s of steering in the small experimental ICF-1 (6 kg). The particles were situated on the surface before steering (like on the left picture).
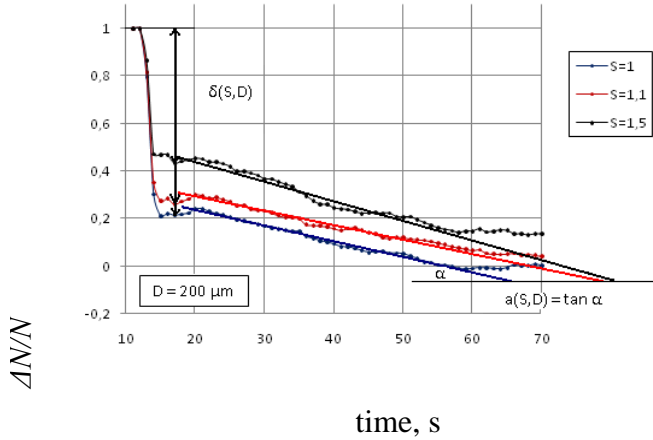
20

Fig. 4. Relative difference of the particle number between the zones of the upper and the lower eddy ΔN/N in ICF-2. Particles with diameter D=200 μm and different liquid-to-particle density ratio S.

Tab. 1. The time of homogenization in laboratory ICF-2. The values are calculated taking into account equations (3-5).

S	D, μm	t_{hom}, s
	50	53±9
1.0	100	52±10
	200	47±11
	50	58±9
1.1	100	57±10
	200	53±13
	50	80±13
	100	82±15
1.5	180	85±19
	190	86±19
	200	86±20

2.4. Conclusions and outlook

The described numerical approach, which is based on the LES Euler-Lagrange simulation of particle laden liquid metal flow in the limit of dilute conditions can be used for the case studies of the behaviour of solid inclusions in ICF. Despite the time consuming simulations of the flow, the regression model for the homogenization of inclusions can be created on the basis of several cases. This model can be used for optimization of design and operation of ICF.

The iron particles can be used as a physical model for the tracking of non-conductive inclusions in ICF. The original experimental results are in a satisfactory agreement with the simulations. The described experimental technique is very useful, because the ferromagnetic particles can be easily separated from the liquid metal with the permanent magnet.
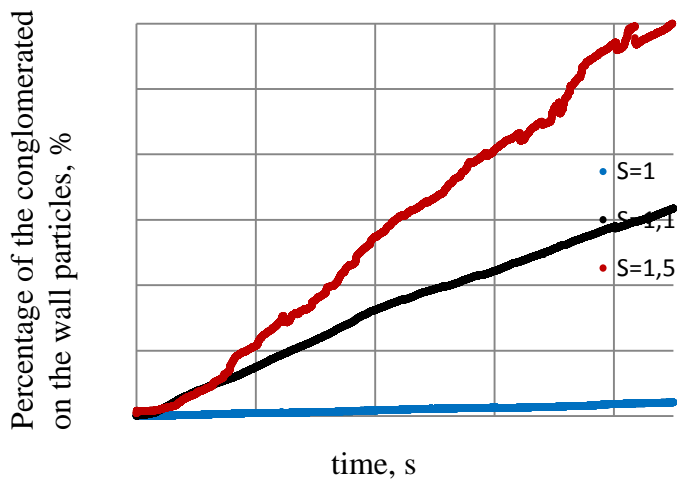
The numerical results of the carbon admixing from the open surface of the steel melt in ICF are in a good qualitative agreement with the industrial observation of the particle dynamics on the surface of the melt. Therefore the calculations can also give a relevant conception of the redistribution of the inclusion in the invisible bulk of the melt.

The estimations show that the average size of the inclusions can significantly increase during the weekend, when the furnace is switched to a lower power regime. This process can ensure the sponge-like clogging. The present estimations confirm the necessity of the particle tracking simulation in CIF, coupled with the size evolution model.

Fig. 5. Percentage of the 200 μm particles, which are conglomerated on the wall of ICF-2.

References

1. **M. Scepanskis, A. Jakovics, B. Nacke, E. Baake**. The simulation of the behavior of alloying admixture particles in the induction crucible furnaces // Heating by electromagnetic sources – Padova, May 2010, pp. 3 – 10.
2. **M. Scepanskis, A. Jakovics, B. Nacke**. The simulation of the motion of solid particles in the turbulent flow of induction crucible furnaces // ECOMASS CFD – Lisbon, June 2010, 15 p. (CD).
3. **M. Scepanskis, A. Jakovics, B. Nacke**. Homogenization of alloying particles in induction crucible furnaces // Modelling for material processing – Riga, Latvia, 2010, pp. 259 - 264.
4. **M. Scepanskis, A. Jakovics.** The Lagrangian particles in the EM driven turbulent flow with fine mesh (the treatment of *solidParticle* library in OpenFoam) // Open source CFD International conference – Munich, Germany, 2010, 10 pp. (CD).
5. **M. Scepanskis, A. Jakovics, B. Nacke.** Homogenization of nonconductive particles in EM induced metal flow in a cylindrical vessel // Magnetohydrodynamics – 2010, Vol. 46, Nr. 4, pp. 413 - 424.
6. **M. Ščepanskis. A. Jakovičs, E. Baake, B. Nacke**. Numerical solution of non-linear Lagrangian equations for inertial particles in turbulent flow // Mathematical modelling and analysis - Sigulda, May 25 – 28, 2011, p. 115.
7. **M. Scepanskis, A. Jakovics, E. Baake, B. Nacke.** The oscillations appering during the process of particle homogenization in EM induced flow of ICF // Fundamental and applied MHD – Borgo, 2011, vol. 2, pp. 653 - 657.
8. **M. Scepanskis, A. Jakovics, E. Baake, B. Nacke.** Development of solidParticle library for the modelling of particle transfer in EM induced turbulent flows. // Multiphysical modelling in OpenFOAM – Riga, October 2011, pp. 21 – 22 and 103 – 106.
9. **M. Scepanskis, A. Jakovics, E. Baake.** Statistical analysis of the influence of forces on particles in EM driven recirculated turbulent flows // Journal of physics: Conference series – 2011, vol. 333, 012015, 14 p.
10. **M. Scepanskis, A. Jakovics, M. Brics, E, Baake, B. Nacke.** Simulation of growth and transportation of solid inclusions in induction furnaces // Proceedings of the 8-th international conference on clean steel – Budapest, 2012, 10 pp. (CD)
11. **M. Scepanskis, A. Jakovics, B. Nacke, E. Baake.** Redistrubution of solid inclusions in the turbulent flow of metallurgica induction furnaces // Turbulencs, heat and mass transfer 7 – Palermo, 2012, p. 1123 – 1126.
12. **M. Scepanskis, A. Jakovics, E. Baake, B. Nacke.** Numerical analysis and experimental verification of the behaviour of solid inclusions in induction crucible furnaces // Journal of iron and steel research international – 2012, vol. 19, suppl. 1, p. 713 - 716.

3. Coupled numerical modeling of conducting liquid turbulent flow and free surface dynamics in alternate electromagnetic field

Introduction

In induction furnaces that are widely applied in metallurgical industry the behaviour of molten metal free surface might be notably unsteady and complicated because of the strongly pronounced nonlinear interaction between electromagnetic (EM) field, melt flow and free surface shape, as well as mean flow instability, turbulence, furnace power switches and etc. In the meantime, requirements for the free surface shape and behavior are specified by the different tasks of particular technological process. Since the problem of free surface shape control appears to be significant for processing of high quality metallic materials (e. g. in conditions of complete and semi-levitation), approach for numerical prediction of molten metal free surface dynamics

22

was developed.

Heat and mass transfer processes in induction furnaces with fixed hydrostatic meniscus [1], as well as considering free surface dynamics in 2D [2], are actively studied numerically. Latest developments in this field succeeded with first results of 3D numerical modelling of liquid droplet dynamics in a high DC magnetic field with simplified k-ω turbulence description [3]. Meanwhile, previous investigations [4] and [5] revealed that in case of induction crucible furnace (ICF) with two characteristic mean flow vortexes only the (Large Eddy Simulation) LES model gives comparable results to experimental measurements.

Meanwhile, the lack of 3D model for numerical calculation of free surface dynamics of melt in an alternate EM field with application of précised LES approach specified the main goal of our research.

3.1. Governing equations

Let us consider electrically conductive melt in a harmonic EM field and introduce the depth of EM field penetration

$$\delta_{EM} = \left(\mu_0 \sigma \pi f \right)^{-1/2}, \tag{2}$$

where μ_0 is magnetic constant, σ is electric conductivity and f is the frequency of harmonic EM field.

On the one hand, the field generates harmonic eddy currents in EM skin layer δ_{EM} that partially dissipate in thermal energy and heat the melt. On the other hand, external and eddy current generated EM field interacts with eddy currents and Lorentz forces are induced in the skin layer of the melt. Let us leave aside the thermal energy generation and heat transfer processes, as well as material property dependence on temperature, and focus mainly on the EM field, free surface shape and hydrodynamic (HD) flow reciprocal interaction (Fig.1.).
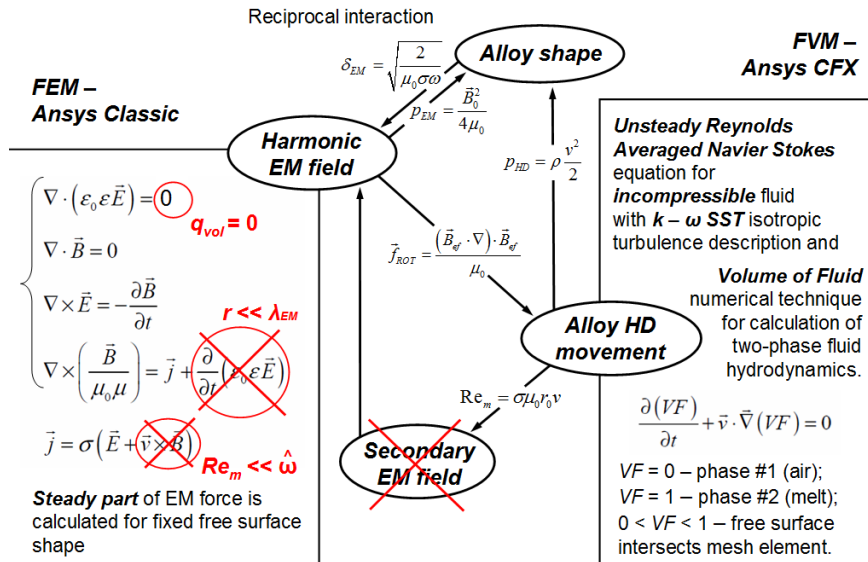

Fig. 1. Model assumptions

Due to harmonic nature both of EM field and induced eddy currents, the Lorentz force f_{EM} can be decomposed into a steady and harmonic part that oscillates with double frequency of EM field [6]

$$\vec{f}_{EM} = \left\langle \vec{f}_{EM} \right\rangle + \vec{\tilde{f}}_{EM} \cdot \cos\left(2\omega t + \varphi \right), \tag{3}$$

where ω is an angular frequency of harmonic EM field and φ is a phase.

Because of much greater inertia times of melt in comparison to the alternate EM field timescale ($f > 50$ Hz), only the steady part of the Lorentz force can be considered.

Moreover, the steady part can be decomposed into a potential and whirling part:

$$\vec{f}_{EM} = -\nabla \left(\frac{\vec{B}_{ef}^2}{2\mu_0} \right) + \frac{1}{\mu_0} \left(\left(\vec{B}_{ef} \cdot \nabla \right) \cdot \vec{B}_{ef} \right) = -\nabla \left(p_{EM} \right) + \frac{1}{\mu_0} \left(\left(\vec{B}_{ef} \cdot \nabla \right) \cdot \vec{B}_{ef} \right). \tag{4}$$

The potential part of Lorentz force can be expressed in terms of EM pressure p_{EM} that squeezes the melt. In the same time, on account of the skin-effect, the shape of conductive fluid reciprocally influences the distribution of EM field.

Meanwhile, the whirling part of Lorentz force corresponds for recirculative flow of melt that on account of HD pressure perturbates the free surface shape and generates the magnetic field itself.

Let us consider a non-dimensional frequency

$$\hat{\omega} = 2\pi f \sigma \mu_0 r_0^2 \tag{5}$$

that shows the relation between the induced and external EM field, and magnetic Reynolds number

$$Re_m = \sigma \mu_0 r_0 v_0 \tag{6}$$

that gives the relation between EM field that is generated by the flow and external EM field.

Combining equations (5) and (6) it can be shown that in typical case of induction furnace

$$\frac{\hat{\omega}}{Re_m} = f \cdot \frac{2\pi r_0}{v_0} \square \ 1, \quad f > 50\,\mathrm{Hz}, \quad r_0 \approx 1\,\mathrm{m}, \quad v_0 \approx 1\,\mathrm{m/s} \tag{7}$$

EM field generated on account of the flow is insignificant in comparison to induced EM field.

Assuming no free charge in the system and neglecting displacement currents (no EM wave radiation) the reduced Maxwell equation system in addition with reduced Ohms law (Fig. 1)and appropriate boundary conditions is solved with finite element method in *ANSYS Classic* and the Lorentz force distribution in melt with particular free surface shape is obtained.

In the HD part of calculation the Navier-Stokes equation for incompressible fluid is solved with finite volume method in *ANSYS CFX*.

In typical cases of ICF the Reynolds number

$$Re = \frac{r_0 v \rho}{\eta} > 10^3 , \tag{8}$$

indicates on fully developed turbulent flow, thus the k-ω SST or LES turbulence models [7] are used additionally.

Volume of Fluid (VOF) numerical technique is applied for calculation of two-phase flow[7]. In VOF technique the phase distribution is represented with scalar volume fraction field $F(x_i, y_i, z_i, t)$. In particular case, $F = 0$ when mesh element is contains only one phase (air) and $F = 1$ when element contains the other phase (melt). Accordingly, when phase surface crosses element - $0 < F < 1$. For phase dynamics the transport equation is solved

$$\frac{\partial F}{\partial t} + \vec{v} \cdot \nabla F = 0 , \tag{9}$$

and free surface is reconstructed as isosurface of $F = 0.5$.

Volume density of surface tension force is calculated as

$$\vec{f}_\gamma = -\gamma \left(\nabla \cdot \vec{n} \right) \vec{n} \delta_\gamma , \tag{10}$$

where γ is surface tension coefficient, $\vec{n}$ is free surface normal and δ_γ is Delta function that ensures that surface tension force is located at free surface.

3.2. Numerical implementation
3.2.1. Hydrostatic model

Numerical calculation of steady state free surface shape in hydrostatic approximation is formulated by coupling of EM calculation in *ANSYS Classic* to a self-written finite difference code for calculation of meniscus that satisfies the pressure balance (11)

$$\rho g h_i = \gamma \left(\frac{1}{r_{1i}} + \frac{1}{r_{2i}} \right) + p_{EMi}, \tag{11}$$

where h is the height of meniscus, r_1 and r_2 main curvature radii, p_{EM} is EM pressure and index i denotes on a particular point of free surface.

Schematic model implementation is presented in Table 1, a.

3.2.2. Hydrodynamic model

Numerical calculation of free surface dynamics of EM induced turbulent flow is arranged by means of *ANSYS Classic* for EM calculation, *ANSYS CFX* for two-phase turbulent flow calculation and their external coupler written by V. Geza. Schematic model implementation is presented in Table 1, b.

Initial free surface shape of molten metal, as well as every transient shape obtained with two-phase HD calculation is written into a file. This file contains free surface keypoint numbers n_i (automatically enumerated by *ANSYS CFX*), keypoint coordinates (x_i, y_i, z_i), and series of keypoint number sequences that indicate the order of free surface keypoint connection with lines for definition of elementary polygons.

Transferring free surface keypoints and elementary polygons from *CFX* to *ANSYS Classic* a self written filtering procedure is performed in order to avoid generation of degenerate surface polygons that have great edge length ratios and cause problems in *ANSYS Classic* volume mesher.

Finally, filtered free surface consisting of elementary triangular non-degenerate areas is obtained and the finite element mesh for EM problem is constructed.
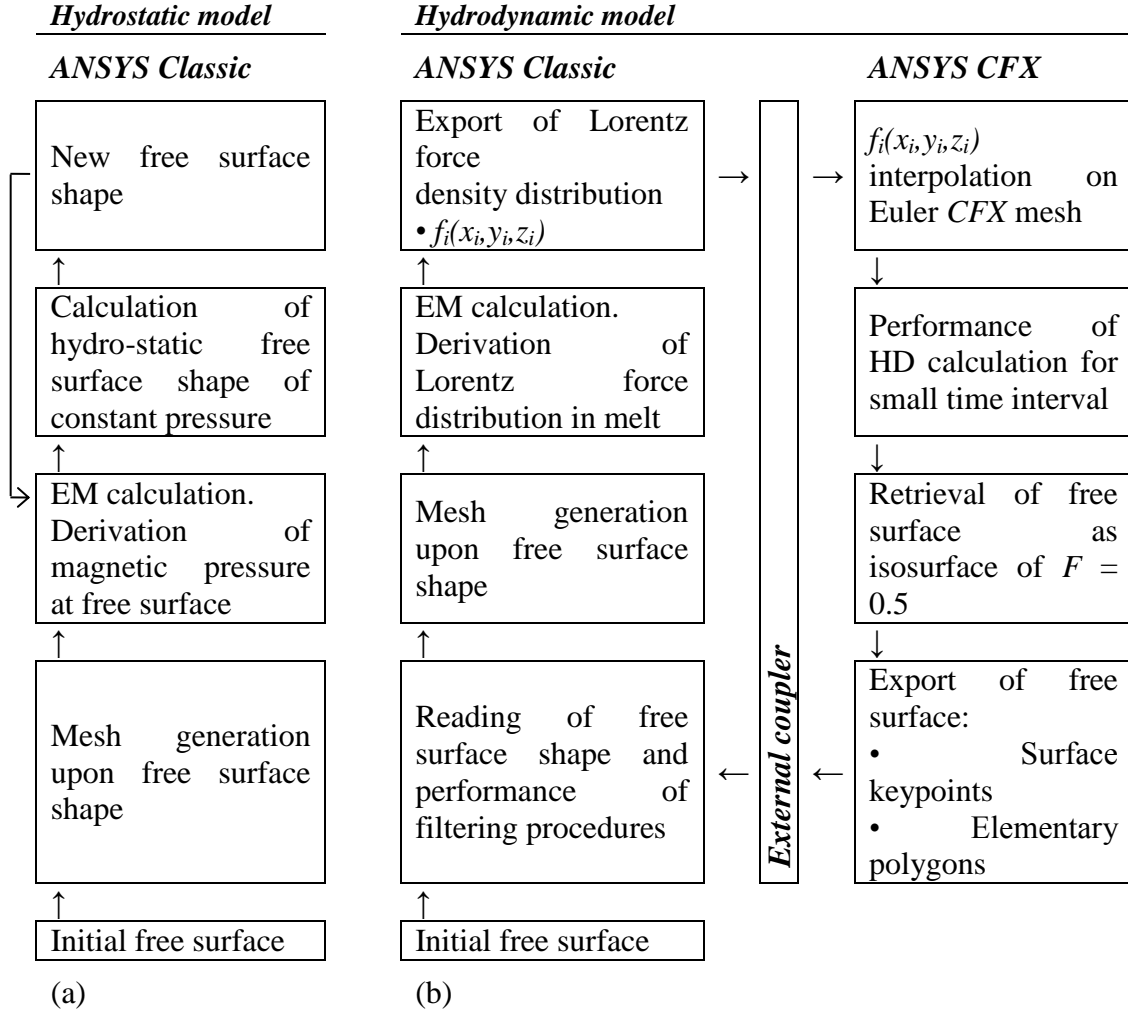
Hydrostatic model	Hydrodynamic model	
ANSYS Classic	ANSYS Classic	ANSYS CFX
New free surface shape	Export of Lorentz force density distribution • $f_i(x_i, y_i, z_i)$ →	→ $f_i(x_i, y_i, z_i)$ interpolation on Euler CFX mesh
↑	↑	↓
Calculation of hydro-static free surface shape of constant pressure	EM calculation. Derivation of Lorentz force distribution in melt	Performance of HD calculation for small time interval
↑	↑	↓
EM calculation. Derivation of magnetic pressure at free surface	Mesh generation upon free surface shape	Retrieval of free surface as isosurface of $F = 0.5$
↑	↑	↓
Mesh generation upon free surface shape	Reading of free surface shape and performance of filtering procedures ←	← External coupler ← Export of free surface: • Surface keypoints • Elementary polygons
↑	↑	
Initial free surface	Initial free surface	
(a)	(b)	

Table 1. Implementation of free surface calculation in (a) - hydrostatic and (b) - hydrodynamic consideration.

In the next step the distribution of harmonic EM field is calculated for the fixed free surface shape of molten metal. The coordinates of alloy mesh element centroids (x_i, y_i, z_i), as well as the values of Lorentz force density components (f_{xi}, f_{yi}, f_{zi}) in alloy mesh centroids are retrieved and written into a file.

In the beginning of the transient HD calculation the Lorentz force density is interpolated on the CFX finite volume mesh and used as a mechanical momentum source in two-phase turbulent flow equations. Then the calculation of unsteady flow is performed for sufficiently small time interval for which the slight change of free surface shape is considered to be not influencing the Lorentz force distribution.

By the end of HD calculation a new transient free surface shape is obtained and written into a file. The recalculation of Lorentz force distribution upon the new free surface shape is performed further and the repeat of whole calculation loop ensures fully automatic free surface dynamics computation.

3.3. Model verification
3.3.1.Steady state free surface

Big laboratory scale ICF. The first verification of developed approach is performed by comparison between experimental measurements [4] of Wood's metal (ρ_{Al} = 9400 kg/m³, σ_{Al} = 10^6 S/m, μ_{Al} = 4.2 mPa·s) steady state meniscus shape in big laboratory scale ICF (Fig. 2), our 2D calculation results and results of 2D steady simulation[8].

Distribution of Lorentz force density (δ_{EM} = 2.57 cm), steady state flow pattern with characteristic two torroidal vortex structure and good agreement between calculated meniscus shape (black line), experimental measurements (points) and O. Pesteanu 2D calculation (red line) is shown in Fig. 2.

Small laboratory scale ICF. Experimental measurements of steady meniscus heights above initial filling (by E. Baake) in small laboratory scale ICF (Fig. 3) were used for the further proof of model accuracy. Calculated quasi steady state velocity pattern (left) and Lorentz force density distribution (right) (δ_{EM} = 2.77 cm), as well as meniscus shape in comparison to the experimental data of meniscus heights above initial flat free surface are presented in (Fig. 3). Experimental measurements are marked by red ticks, while the ticks vertical lines correspond for the given measurement errors due to the turbulence and mean flow instability that caused free surface fluctuations.

IFCC. Experimental measurements of aluminum melt (ρ_{Al} = 2300 kg/m³, σ_{Al} = 3.6·10^6 S/m, μ_{Al} = 1.29 mPa·s) free surface shape in laboratory scale induction furnace with cold crucible (IFCC) [9] were used for further verification. On account of the symmetry of the setup the EM calculation was performed only for one section considering azimuthal inhomogeneity of EM field due to the sectioned crucible (Fig. 4). Air gap of 1 mm was ensured between the melt, the bottom and the crucible walls due to the great electrical resistivity of the skull that appears in the regions of contact between the melt and water-cooled crucible.

The comparison between the measured and calculated free surface shapes of aluminum melt in IFCC at different initial fillings and inductor effective currents (Fig. 4) revealed a fine correlation between the model prediction and experiment both for meniscus total height above the bottom and meniscus shape.

Single frequency EM levitation melting device. The next step of developed model verification is based on comparison to experimental measurements and 2D steady simulation results of aluminum melt levitation in a single frequency EM levitation melting device[8],[10]. This EM levitation furnace consisted of ferrite yoke and copper inductor with 16 turns (Fig. 6). Quartz tube is placed in the air gap between yoke ends and inductor coils in order to prevent unexpected contact between the melt and furnace parts.
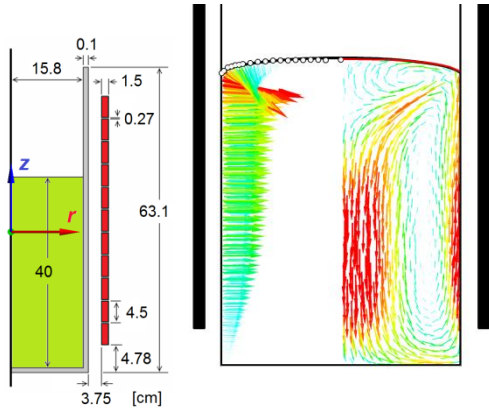
Fig. 2. Big ICF, calculated f_{EM} (left) and velocity (right), meniscus measurements (points)[4], our model (black line) and O. Pesteanu calculation (red line)[8].
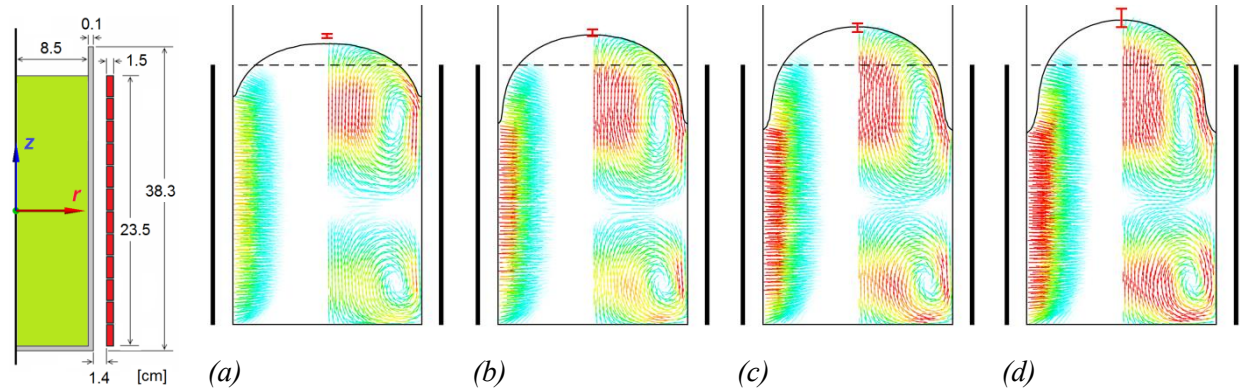
Fig. 3. Geometry of small ICF, calculated f_{EM} (left) and flow pattern (right) and comparison between experimentally measured meniscus heights (ticks) and calculated (solid line) steady state free surface for initial filling of 100% and different I_{ef}: (a) $I_{ef} = 1753$ A; (b) $I_{ef} = 2020$ A; (c) $I_{ef} = 2262$ A; (d) $I_{ef} = 2464$ A.

$f_{EM}, \cdot 10^5 N/m^3$
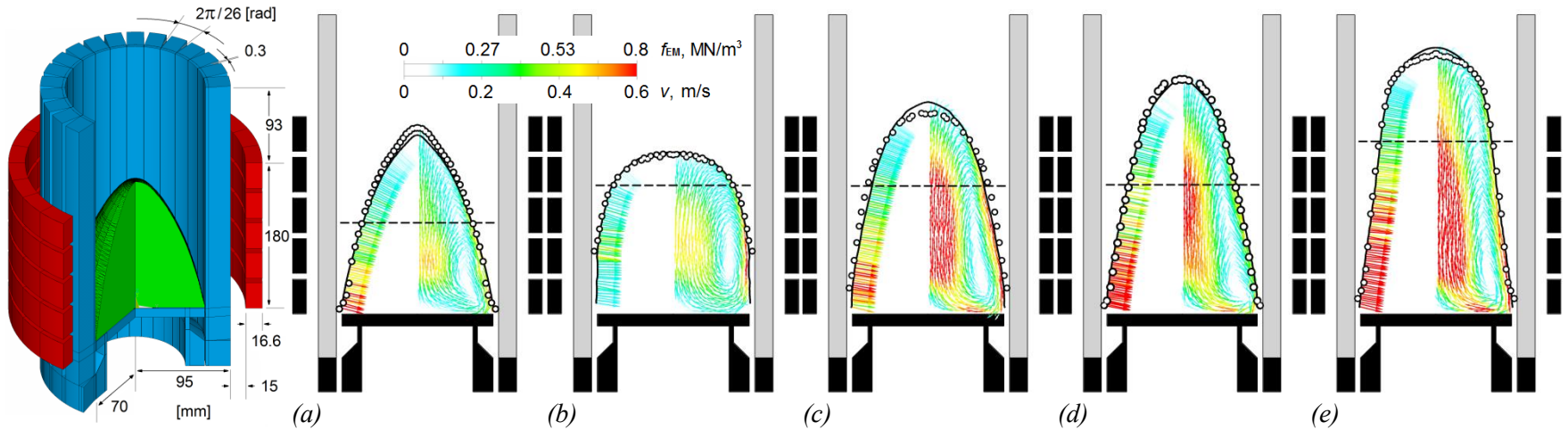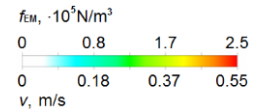
Fig. 4. IFCC model, calculated Lorentz force density f_{EM} (left) and flow pattern (right), and comparison between experimentally measured (points) [9] and calculated (solid line) steady state free surface shapes for different initial fillings (dashed line) in respect to inductor height and effective inductor currents I_{ef}: (a) IF = 46%, $I_{ef} = 3154$ A; (b) IF = 65%, $I_{ef} = 1929$ A; (c) IF = 65%, $I_{ef} = 2956$ A; (d) IF = 65%, $I_{ef} = 3566$ A; (e) IF = 87%, $I_{ef} = 3789$ A.

The comparison between our 3D calculation results for steady state free surface (red line), experimental measurements of droplet position (points) and 2D steady calculation of O. Pesteanu (blue line) proves our 3D model accuracy (Fig. 5). Moreover, qualitative comparison indicates on a nice agreement for free surface shape in experiment and 3D calculation (Fig. 7).

Eventually the verification of developed model has been successfully completed for the case of two ICFs, IFCC with several highly pronounced meniscus and EM levitation melting device and evidently approved the accuracy of developed numerical approach.
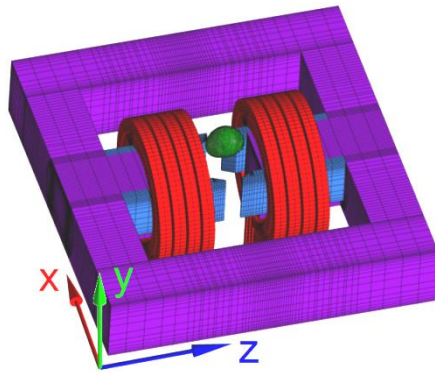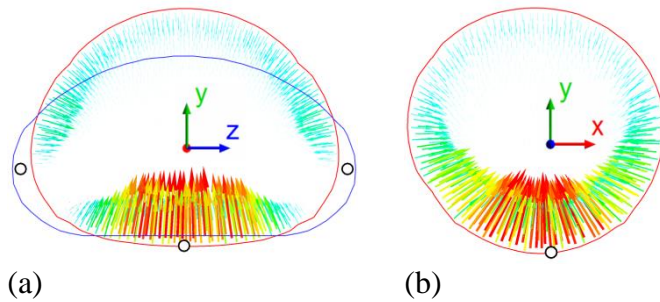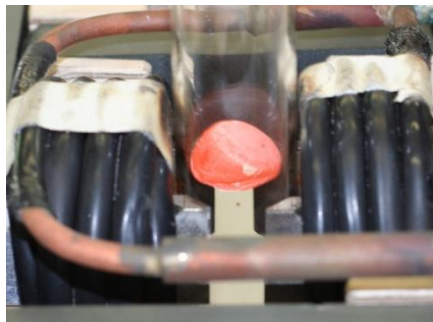

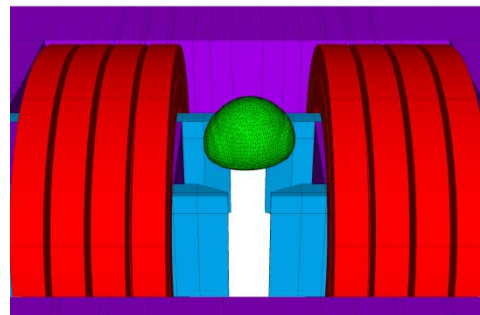Fig. 6. Single frequency EM levitation melting device.

(a)   (b)

Fig. 5. 3D calculation results for Lorentz force density (0-3·10^5 N/m^3) and free surface shape (line) in comparison to O. Pesteanu 2D calculation (blue line) and his experimental measurements (points).

(a)   *(b)*

Fig. 7. Qualitative comparison between experimentally observed [10] (a) and numerically predicted (b) free surface shape of EM levitating drop.

3.3.2. Free surface dynamics in big industrial ICF

Big industrial scale ICF (inner crucible radius $r_0 = 0.43$ m) with geometry adopted from [11], 100% filling of aluminum melt in respect to inductor height, inductor current of 2 kA and typical current frequency of 50 Hz is considered.

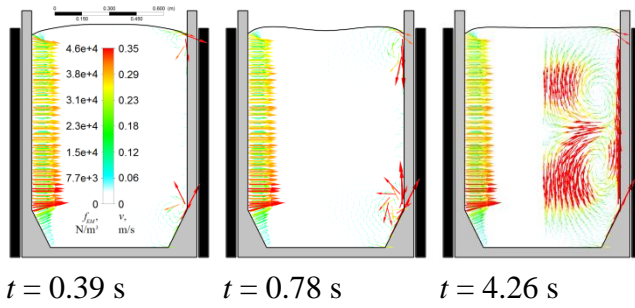$t = 0.39$ s $t = 0.78$ s $t = 4.26$ s

Fig.8. 2D calculation results for Lorentz force density (left), flow pattern (right) and free surface dynamics at different time moments in big industrial ICF.
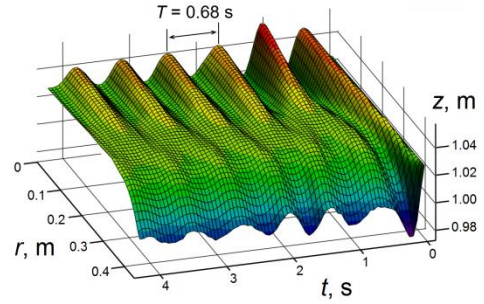
Fig. 9. 2D calculation results for molten aluminum free surface dynamics in industrial ICF, free surface oscillation period $T_{calc} = 0.68$ s.

It is assumed that at initial time moment of $t = 0$ s the surface of molten aluminum is flat and inductor is instantly fed with AC. In industrial cases inductor current values are also changed in steps, despite that such extreme situation when current value is switched from $I = 0$ to $I = I_{max}$ is not common. Meanwhile, the inverse situation takes place switching off the furnace and for numerical approach validation particular numerical experiment has an industrial background.

2D transient calculation results for Lorentz force density distribution, developing flow pattern and free surface shapes at particular time moments are shown in Fig. 8..

In particular furnace the symmetric localization of inductor in respect to aluminum melt contributes to development of two equal torroidal vortexes. Due to the small power density the free surface oscillation amplitude is less than 4% in respect to the height of initial filling and can be described with small amplitude approximation. Oscillations of free surface have a tiny effect on the Lorentz force distribution, as well as have a small influence on the flow pattern.

The dynamics of free surface profile sketches regular oscillations with typical period $T_{calc} = 0.68$ s (Fig 9). Analytical approximation of free surface oscillation period accordingly to [11] gives the value of

$$T_{analyt} = 2\pi \left(r_0 / \lambda_1 \cdot g \right)^{1/2} \cdot \tan \left(\lambda_1 \cdot h_0 / r_0 \right) = 0.676 \text{ s} , \qquad (12)$$

where λ_1 is Bessel's function 1st solution, g = 9.81 m/s^2 and h_0 is the height of initial filling.

The difference between numerically calculated and analytically estimated free surface oscillation period appears to be less than 1%.

3.4. EM levitation in 2D consideration

A system of two inductor turns and alloy drop at initial conditions of spherical shape and zero velocity is considered (Fig.10). The aim of particular 2D numerical experiment was to entrap the alloy and obtain a stable EM levitation. The design of setup and operational parameters were not adopted from any experimental data, as well as, were not optimized and this is the reason for exaggerated inductor current values used.

A fine timestep of 0.1 ms for Lorentz force recalculation due to the free surface shape change, as well as fine space discretization of 0.1 mm both for EM ($\delta_{EM} = 2.3$ mm) and HD calculation was applied.

30

Initial disbalance between gravity and EM forces causes the drop to move down for the first 40 ms (Fig. 11). The laminar flow ($Re = 700$) rapidly develops and one torroidal vortex with downward velocity on the drop symmetry axis is generated. During vortex formation the drop stretches twice in axial direction, however, reaching the quasi steady state the free surface gains characteristic "spinning-top" shape and axial and radial dimensions remain comparable.

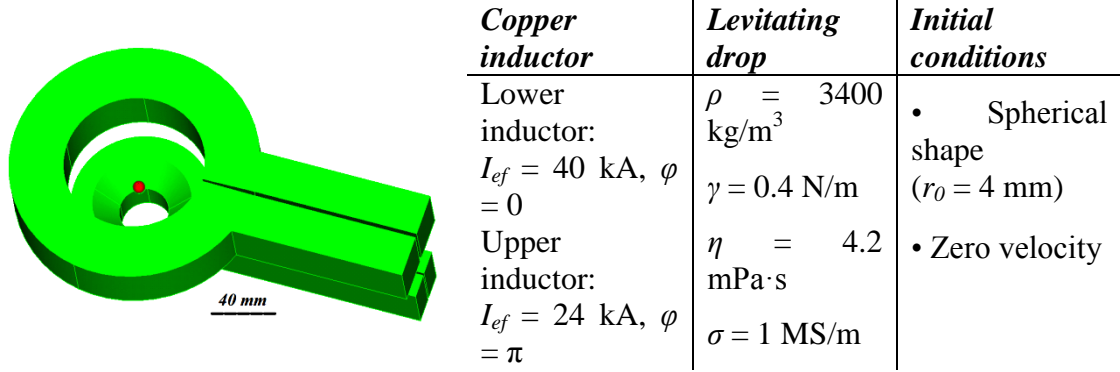| Copper inductor	Levitating drop	Initial conditions
Lower inductor: $I_{ef} = 40$ kA, $\varphi = 0$	$\rho = 3400$ kg/m^3 $\gamma = 0.4$ N/m	• Spherical shape ($r_0 = 4$ mm)
Upper inductor: $I_{ef} = 24$ kA, $\varphi = \pi$	$\eta = 4.2$ mPa·s $\sigma = 1$ MS/m	• Zero velocity

Fig. 10. Geometry and parameters for numerical experiment of droplet EM levitation.
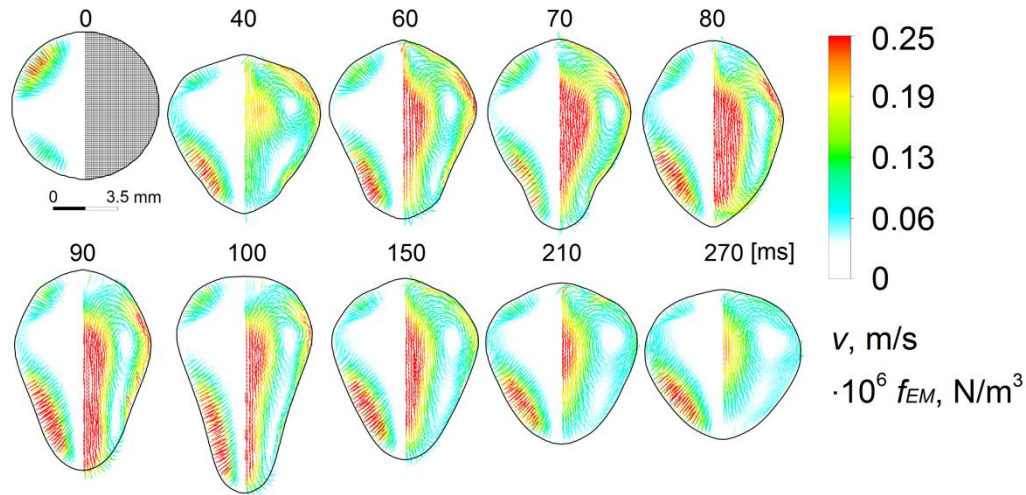

Fig.11. Lorentz force density distribution (left), instantaneous velocity pattern (right) and free surface shape of levitating drop at particular time moments obtained with transient calculation of 2D hydrodynamic model.

3.5. Parameter studies
3.5.1. 2D steady state free surface with hydrostatic model

Inductor effective current. Greater current values in ICF lead to greater meniscus shape deformations defined by greater EM pressure drops between symmetry axis and inner wall of crucible. Magnetic field squeezes the alloy and meniscus height and free surface area increases (Fig. 12, a).

AC frequency. Increase of AC frequency leads to decrease of EM field penetration depth δ_{EM} (2) and a sharp surface deformation is obtained only closer to the crucible wall, while on the symmetry axis free surface remains flat and the height of meniscus decreases (Fig. 23, a).

On the other hand, decreasing AC frequency leads to situation when alloy can be considered as an absolutely transparent for EM field and on free surface do not appear notable gradients of EM pressure that cause surface deformations.

Hence, a particular AC frequency exists for which the meniscus height is the greatest [12].

Surface tensions. For clean molten metal surface the impact of surface tension on meniscus shape in ICF is negligible. However, in some cases surface tension coefficient of alloy may significantly differ from expected value due to the oxide layer that might appear on the surface. Such layer acts like an elastic membrane and causes increase of surface tension.

The effect of surface tension coefficient on meniscus shape for *I* and *f* held constant can be obtained from Fig. 23, c. Increase of surface tension coefficient γ leads to decrease of free surface area and meniscus height.

Particular results illustrate only the qualitative trend, because surface tension term in pressure balance (11) solved in hydrostatic model was considered in a rather simplified form $\gamma \left(\dfrac{1}{r_1} + \dfrac{1}{r_2} \right) = \gamma \left(\dfrac{\partial^2 z}{\partial r^2} + 0 \right)$ in order to linearize the system of equations and use the direct solver.

Crucible filling. Increase of molten metal relative filling (ratio between initial height of melt and inductor height) with other parameters held constant leads to meniscus shape specific deformation (Fig. 23, d). Due to the finite height of inductor in case of greater relative filling the meniscus expands to regions with lower EM field intensity and becomes flat on the symmetry axis with sharper free surface slope next to the crucible wall.
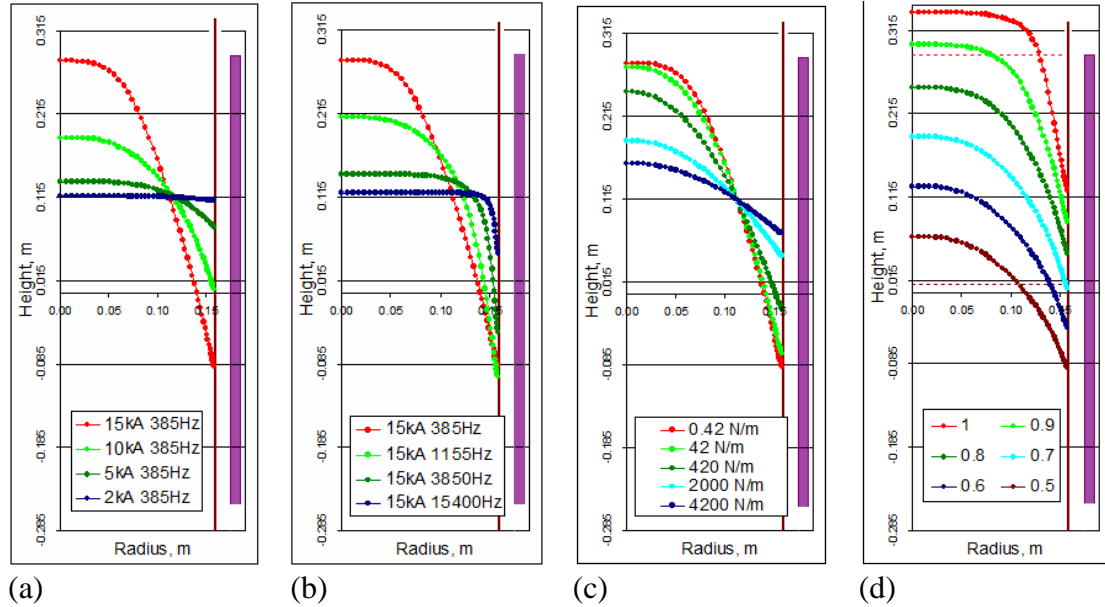

(a) (b) (c) (d)

Fig. 12. Meniscus steady state shapes of Wood's metal in big ICF at different (a) – effective current I_{ef}, (b) – frequency f, (c) – surface tension γ and (d) – initial filling in respect to inductor height calculated with 2D hydrostatic model (all the rest parameters held constant).

3.5.2. 2D free surface dynamics with hydrodynamic model

Inductor effective current. It is considered that the crucible of big ICF (Fig. 2) is filled with melt (ρ = 9400 kg/m^3, η = 10^{-2} Pa·s, zero initial velocity and flat free surface) and at t = 0 s inductor is instantly fed with AC current (f = 385 Hz). Three cases of effective current value I_{ef} are considered: 3 kA, 4 kA and 5 kA.

Lorentz force density distribution, instantaneous flow pattern and free surface shapes at different time moments illustrate the dynamics of the process for the case of

greatest and lowest I_{ef} (Fig. 13). As expected, greater Lorentz force density, free surface oscillation amplitude, flow velocity and quasi steady state (at $t = 3$ s) meniscus height is obtained for greatest current value.

Free surface oscillations on the symmetry axis (Fig. 14) indicate on the same response, moreover, free surface oscillation period, especially for smaller current values (smaller oscillation amplitude) appears to be in good agreement with analytical estimation ($T_{theor} = 0.39$ s) according to[11].
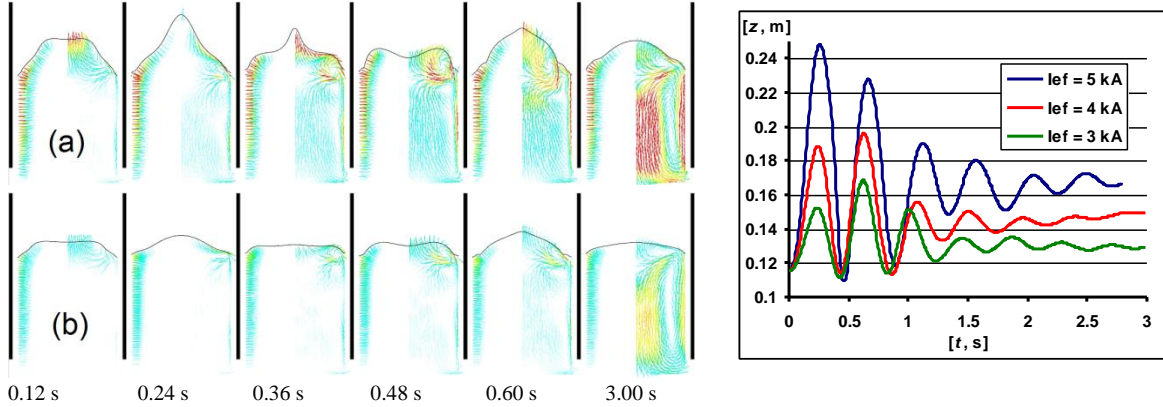

| 0.12 s | 0.24 s | 0.36 s | 0.48 s | 0.60 s | 3.00 s |

Fig.13. Lorentz force distribution on the left (0-3·10⁶ N/m³) and flow pattern on the right (0-0.7 m/s), as well as free surface shape for (a) - $I_{ef} = 5$ kA and (b) - $I_{ef} = 3$ kA.

Fig. 14.Free surface oscillations on the symmetry axis for the case of different effective current values.

Dynamic vuscosity. It is considered that the crucible of big ICF is filled with the same melt and at $t = 0$ s inductor is instantly fed with AC current ($f = 385$ Hz) with effective value of $I_{ef} = 5$ kA. Free surface dynamics is calculated for three cases of melt dynamic viscosity η: 10^{-2} Pa·s, 1 Pa·s and 10^2 Pa·s.

Lorentz force density distribution, instantaneous flow pattern and free surface shapes illustrate the dynamics of the process (Fig. 15).

For the case of greatest dynamic viscosity ($\eta = 10^2$ Pa·s) the quasi steady state regime of flow and meniscus shape is obtained rapidly. Maximal velocity value is up to 10 times less than in case of $\eta = 1$ Pa·s.

For the case of two least viscosity values the dynamics of free surface and flow development look the same. Meanwhile, free surface oscillations on the symmetry axis (Fig. 16) indicate that free surface oscillations for $\eta = 10^{-2}$ Pa·s are damped faster than in the case of $\eta = 1$ Pa·s.

For the case of $\eta = 10^{-2}$ Pa·s the turbulent flow develops rapidly and the maximal value of turbulent (eddy) viscosity is over 15 Pa·s, meanwhile, for the case of $\eta = 1$ Pa·s – the maximal value of turbulent viscosity is only below 10 Pa·s. This means that for $\eta = 10^{-2}$ Pa·s the total viscosity (dynamic + turbulent) is greater and that is why free surface oscillations are damped faster.

It can also be concluded that the height of meniscus point on symmetry axis obtained with hydrodynamic model (with relatively small η – red and blue lines) is greater for 1 cm than calculated with quasi hydrostatic (with great dynamic viscosity – green line) model (Fig. 16).
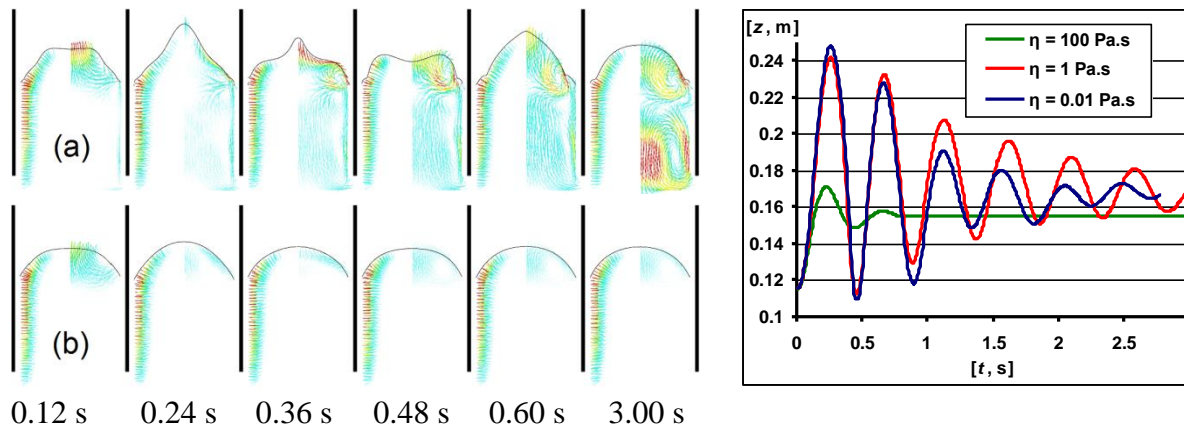
33

0.12 s   0.24 s   0.36 s   0.48 s   0.60 s   3.00 s

Fig. 15. Lorentz force distribution on the left (0-3·10⁶ N/m³)
and flow pattern on the right (0-0.7 m/s), as well as free
surface shape for the case of (a) - η = 1 Pa·s and (b) - η =
100 Pa·s.

Fig. 16. Free surface oscillations on
the symmetry axis for the case of
different dynamic viscosity values.

AC frequency. It is considered that the crucible of big ICF is filled with melt (ρ = 9400 kg/m³, $\eta = 10^{-2}$ Pa·s, zero initial velocity and flat free surface) and at $t = 0$ s inductor is instantly fed with AC current with effective value of $I_{ef} = 3$ kA and different AC current frequencies f: 50 Hz ($\delta_{EM} = 7.1$ cm), 385 Hz ($\delta_{EM} = 2.6$ cm) and 4000 Hz ($\delta_{EM} = 0.8$ cm). The HD VOF calculations are performed on the same mesh with 10 element resolution of the smallest skin depth $\delta_{EM} = 0.8$ cm.

Lorentz force density distribution, instantaneous flow pattern and free surface shapes illustrate the dynamics of the process (Fig. 17). As expected, for the case of $f = 4000$ Hz Lorentz forces appear to be strictly perpendicular to the surface of the melt due to the very small δ_{EM}. Moreover, after 3 s the flow is still developing, while the steady state flow is already achieved for the cases of 50 Hz and 385 Hz.

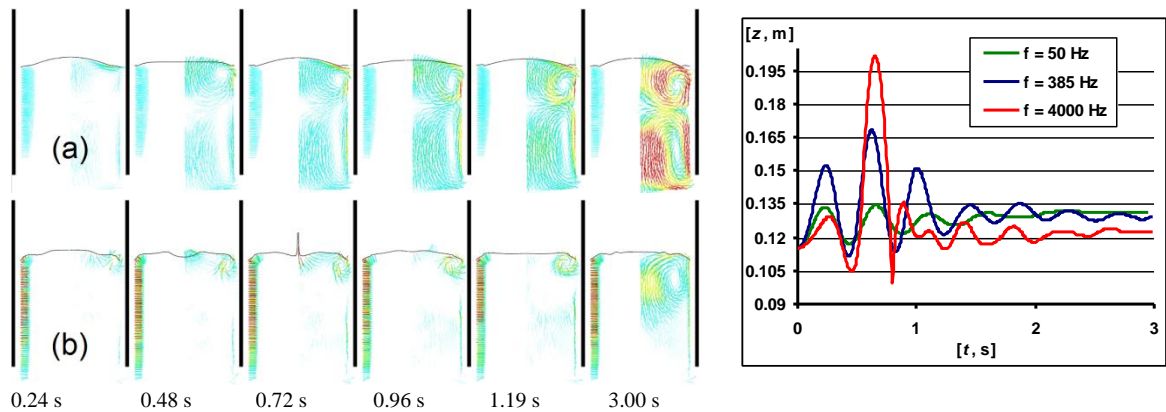0.24 s   0.48 s   0.72 s   0.96 s   1.19 s   3.00 s

Fig. 17. Lorentz force distribution on the left (0-1.5·10⁶
N/m³)
and flow pattern on the right (0-0.45 m/s), free surface
shape for (a) - f = 50 Hz and (b) - f = 4000 Hz.

Fig. 18.. Free surface oscillations on
the symmetry axis for the case of
different AC frequency values.

Like for the meniscus height dependence on AC current frequency, there is a particular frequency for which the greatest melt velocity values can be obtained.

The maximal velocity values for the case of $f = 385$ Hz (Fig. 13. b) and $f = 50$ Hz (Fig. 17, a) are almost the same, however, the flow pattern differs significantly due to the fact, that for smaller frequency the melt is more transparent for EM field rather than for the case of greater frequency. For greater frequencies the EM field is squeezed out of the melt and reciprocal interaction between melt shape and EM field becomes more significant. This fact influences distribution of Lorentz forces that contribute to formation of the steady state flow pattern.

Free surface oscillations on the symmetry axis (Fig. 18) indicate that greater EM field frequencies lead to greater initial perturbation (greater Lorentz force densities are acting on smaller masses due to the smaller δ_{EM}) and highly pronounced nonlinearity of free surface behavior that can not be described with simplified analytical estimations.

3.5.3. 3D free surface dynamics with hydrodynamic model

Inductor effective current. It is considered that the crucible of big ICF (Fig. 2) is filled with Wood's metal (zero velocity and flat free surface) and at $t = 0$ s inductor is instantly fed with AC current with effective value of $I_{ef} = 5$ kA[13].
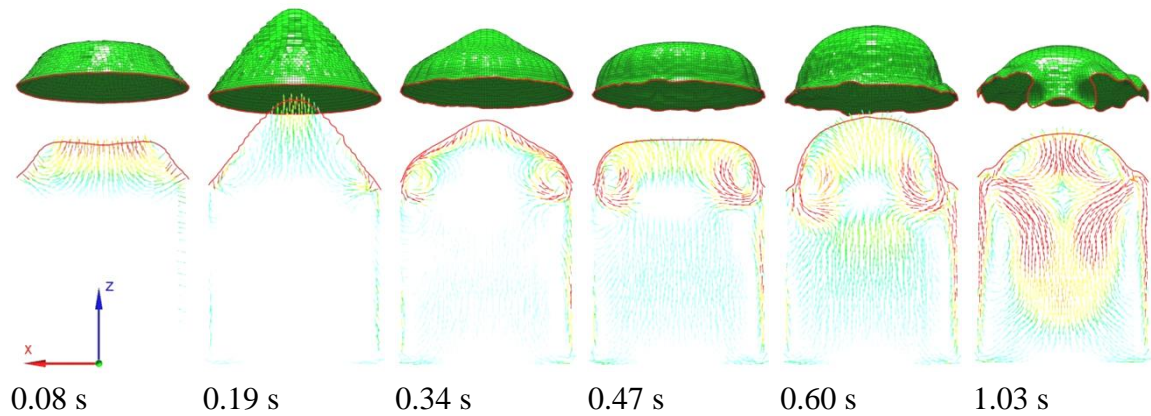

| 0.08 s | 0.19 s | 0.34 s | 0.47 s | 0.60 s | 1.03 s |

Fig. 19.. Flow development (0-0.55 m/s) and free surface oscillations obtained with 3D k-ω SST transient calculation at different time moments for the case of big ICF operating at $I_{ef} = 5$ kA.
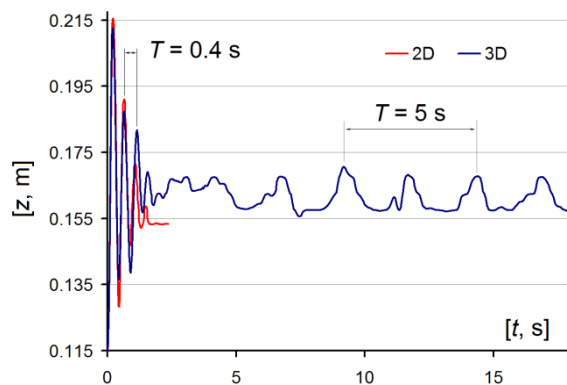

Fig. 20. Oscillations of free surface on the symmetry axis of big ICF for the case of 5kA obtained with 2D (red line) and 3D (blue line) models.

Flow development and free surface states at different time moments illustrate the dynamics of the process (Fig. 19).

The first 2 s of flow calculated with 2D and 3D models (Fig. 20– red and blue lines accordingly) indicate on similar behavior of free surface point oscillations on Z axis. Moreover, the period of these free surface damping oscillations ($T_{calc} = 0.4$ s) is in good agreement with small-amplitude theoretical estimation ($T_{theor} = 0.39$ s) from[11].

The next 4 s correspond to the flow transition to quasi steady state regime and development of turbulence.

Starting approximately from $t = 6$ s the fully developed turbulent flow starts to oscillate with periodical reallocation of upper and lower torroidal vortex. Free surface

shape, EM field and melt flow reciprocal interaction contributes to meniscus regular staggering with typical period of 5 s (Fig. 21).
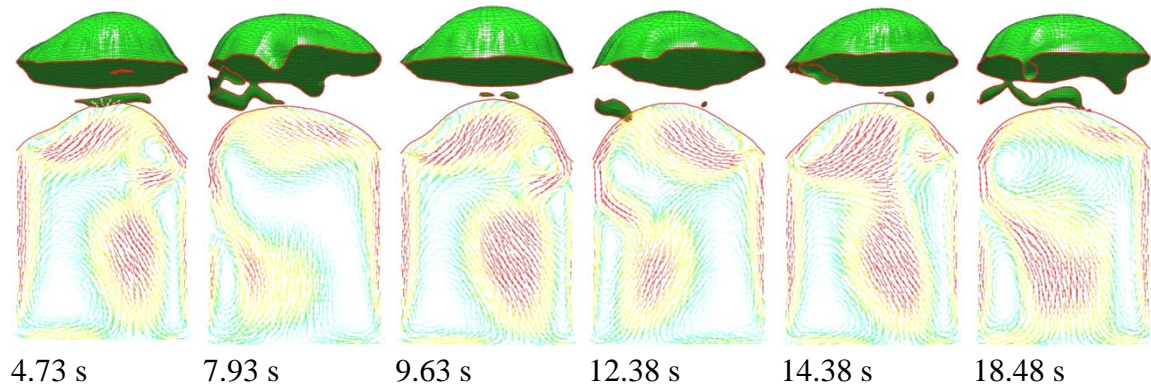

| 4.73 s | 7.93 s | 9.63 s | 12.38 s | 14.38 s | 18.48 s |

Fig. 21. Quasi steady state regime flow patterns (0-0.55 m/s) and free surface shapes obtained with 3D k-ω SST transient calculation for the case of big ICF operating at I_{ef} = 5 kA.

Higher meniscus height and maximal velocity values, as well as, low frequency quasi steady state free surface oscillations are also obtained for the case of greater inductor current I_{ef} = 7 kA (Fig. 22). For this free surface calculation, the same as for the previous one, Lorentz force was recalculated upon new free surface shape every 0.05 s. The calculation was performed for 10 s of flow and took 3 months of computational time on 4 kernel machine (3.4 GHz, 8 Gb RAM).

3.4.5. LES and k-ω SST turbulence model impact on free surface

In comparison to the mean flow and smooth meniscus obtained with transient 3D k-ω SST calculation (Fig. 23, c) the smaller flow structures resolved with LES on account of dynamic pressure contribute to meniscus perturbations on a smaller spatial scale (Fig. 23, b) and, as expected, are in better qualitative agreement with experimentally observed meniscus (Fig. 23, a).

Comparison of instantaneous flow patterns obtained with LES and k-ω SST models (Fig. 24) illustrate the difference between small scale turbulent structures resolved with LES and smooth unsteady Reynolds-averaged flow obtained with k-ω SST.
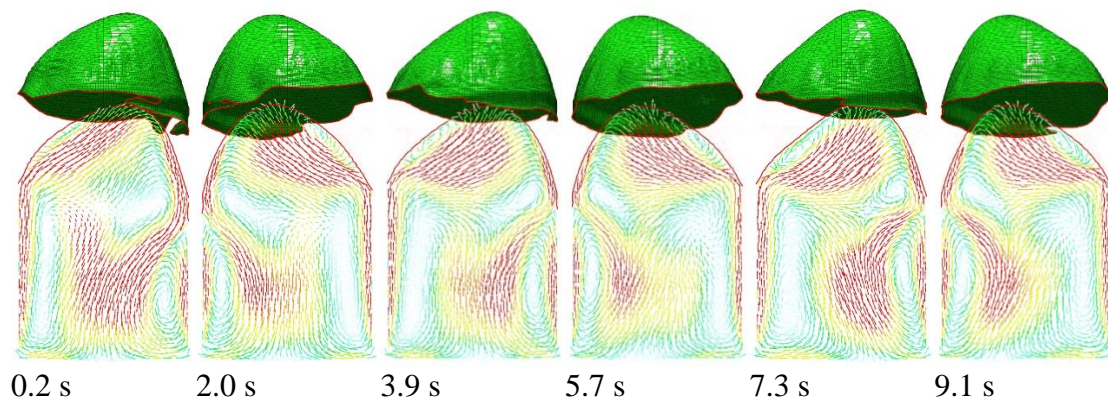

| 0.2 s | 2.0 s | 3.9 s | 5.7 s | 7.3 s | 9.1 s |

Fig. 22. Quasi steady state regime flow patterns (0-0.65 m/s) and free surface shapes obtained with 3D k-ω SST transient calculation for the case of big ICF operating at I_{ef} = 7 kA.
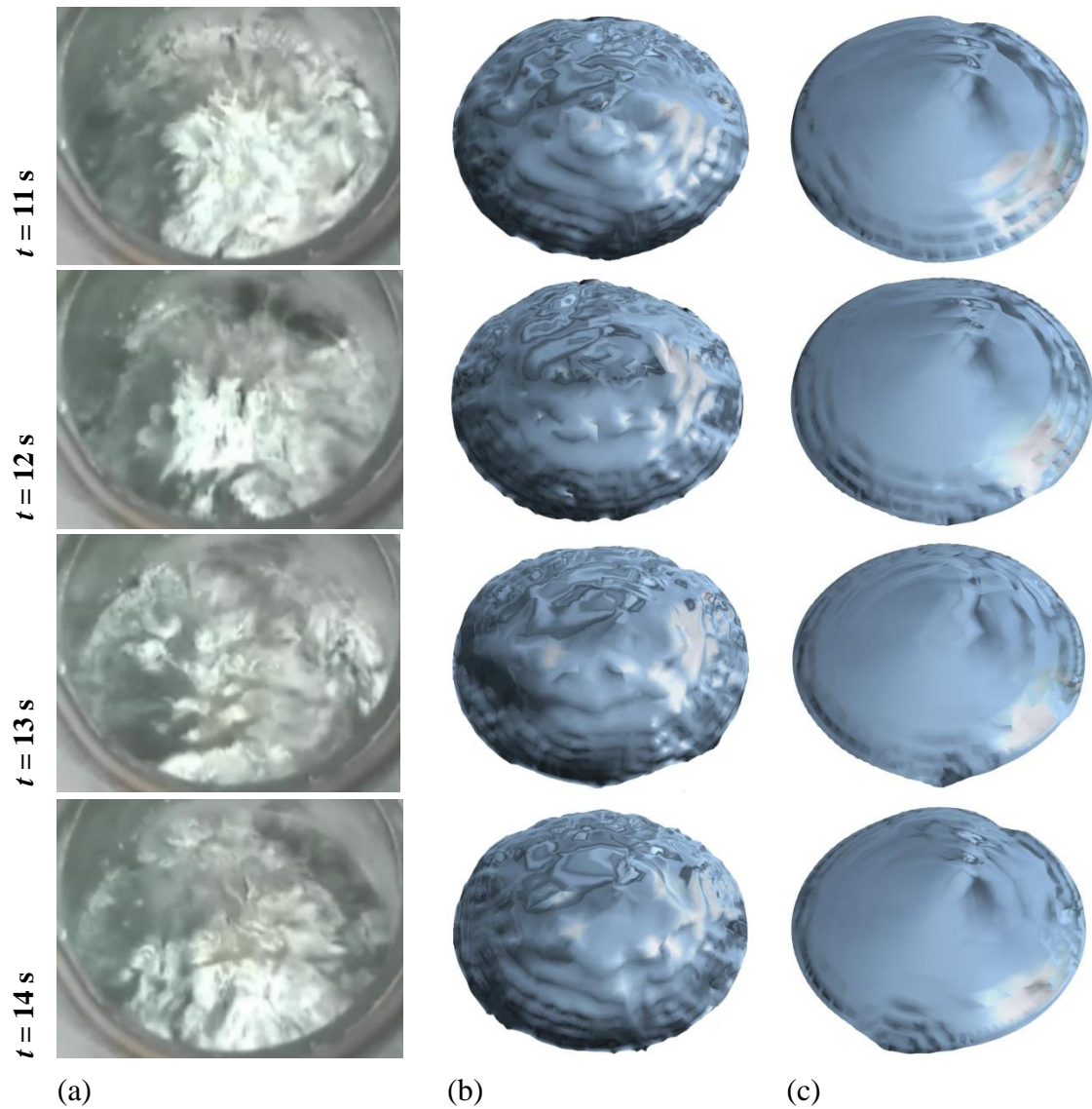
Fig. 23. Qualitative comparison between experimental observations of quasi steady state free surface dynamics in small ICF (a) and numerical simulation of free surface dynamics at quasi steady state regime in big ICF using (b) – LES turbulence model and (c) – k-ω SST model.
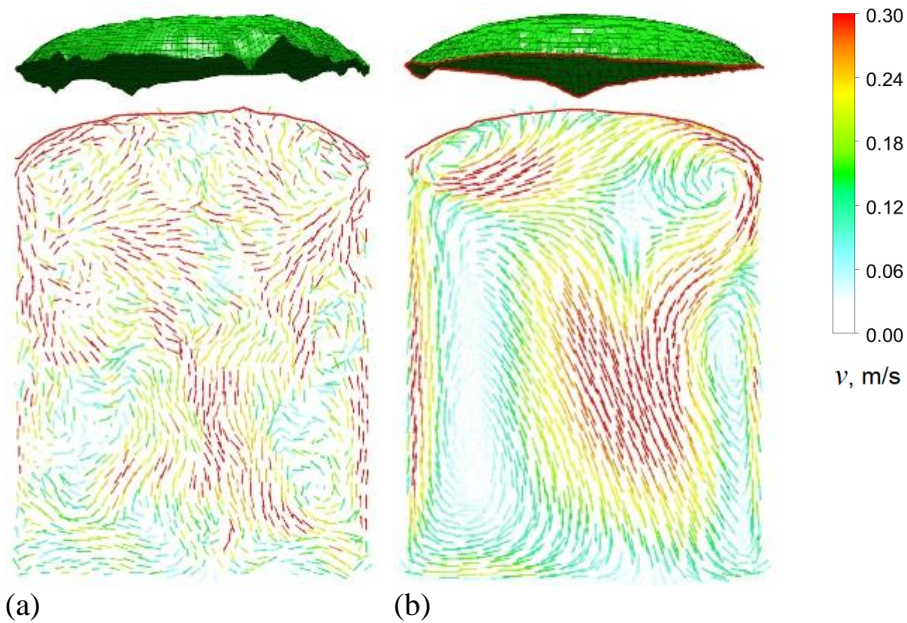
Fig. 24. Instantaneous velocity pattern and free surface shape for the quasi steady state flow regime calculated using (a) – LES turbulence model and (b) – k-ω SST model.

Conclusions

3D consideration, as well as greater inductor current (splashing) and frequency values (strongly pronounced free surface shape and EM field interaction) signify the non-linear effects of free surface dynamics and make impossible the application of simplified analytical estimations for free surface dynamics description. This increases the demand on numerical models that are capable of providing precise solutions for wider parameter scales.

Two-dimensional model for numerical calculation of free surface dynamics of melt in an alternate EM field is developed on account of external coupling of *ANSYS Classic* and *ANSYS CFX*. The model is adjusted for the case of EM levitation and extended on full 3D consideration.

The comparison of our k-ω SST calculation results to appropriate experimental measurements and results of other models for the steady state free surface in induction crucible furnace, induction furnace with cold crucible and EM levitation melting setup, as well as comparison of free surface small amplitude oscillation period to analytical estimation, revealed good correlation and approved accuracy of developed approach.

The performed parameter studies briefly illustrated possibilities of tailoring the EM field by adjusting the design of inductor, AC effective value and frequency etc. in order to achieve suitable shape of free surface and the best performance for EM processing.

References
[1] **A. Umbrasko, E. Baake, B. Nacke, A. Jakovics.** Numerical studies of the melting process in the induction furnace with cold crucible. *Heating by Electromagnetic Sources-07*, Padua, Italy, June 19-22, 2007. Book of abstracts. p. 277-284.
[2] **V. Bojarevics, R. A. Harding, K. Pericleous, M. Wickins.** The development and experimental validation of a numerical model of an induction skull melting furnace. *Metallurgical and Materials Transactions*, 2004, N35B, pp. 785-803.

[3] S. Easter, V. Bojarevics, K. Pericleous. Numerical Modelling of Liquid Droplet Dynamics in Microgravity. *Journal of Physics: Conference Series*, 2011, 327, 012027.

[4] E. Baake. Grenzleistungs – und Aufkohlungsverhalten von Induktions-Tiegelöfen. Doktor-Ingenieur Dissertation, Dusseldorf, 1994, 167 S.

[5] M. Kirpo. Modeling of turbulence properties and particle transport in recirculated flows. Ph.D. Thesis, University of Latvia, Riga, 2008, 184 p.

[6] Y. Fautrelle, A. Sneyd, J. Etay. Effect of AC magnetic fields on free surfaces. *Fluid mechanics and its applications*, 2007, Vol.80, part IV, pp. 345-355.

[7] H. K. Versteeg, W. Malalasekera. *Computational fluid dynamics. Second edition.* Glasgow. Pearson Education Limited, 2007, p. 40-115.

[8] O. Pesteanu, E. Baake. The multicell Volume of Fluid (MC-VOF) method for free surface simulation of MHD flows. Part I: Mathematical model. *ISIJ International*, 2011, Vol.51, N5, pp. 707-713.

[9] E. Westphal. Elektromagnetisches und thermisches Verhalten des Kaltwand-Induktions-Tiegelofens. Doktor-Ingenieur Dissertation, Dusseldorf, VDI Reihe 21 Nr. 210, 1996, 138 S.

[10] O. Pesteanu, E. Baake. The multicell Volume of Fluid (MC-VOF) method for free surface simulation of MHD flows. Part II: Experimental verifications and results. *ISIJ International*, 2011, Vol.51, N5, pp. 714-721.

[11] F. Hegewaldt, L. Buligins, A. Jakowitsch. Transient bath surface bulging at energization of an induction-type crucible furnace. *Elektrowärme international*, 1993, N1, S. 28-42.

[12] S. Spitans, A. Jakovics, E. Baake, B. Nacke. Numerical modelling of free surface dynamics of conductive melt in the induction crucible furnace. *Magnetohydrodynamics*, 2010, 46, pp. 317-328.

[13] S. Spitans, A. Jakovics, E. Baake, B. Nacke. Numerical modelling of free surface dynamics of melt in an alternate electromagnetic field. *Magnetohydrodynamics*, 2011, N4, pp. 461-473.